

A Climatology of Indirect Tropical Cyclone Interactions in the North Atlantic and Western North Pacific Basins

KEVIN C. PRINCE AND CLARK EVANS

Atmospheric Science Program, University of Wisconsin–Milwaukee, Milwaukee, Wisconsin

(Manuscript received 14 November 2019, in final form 23 July 2020)

ABSTRACT

While it is understood that a recurring tropical cyclone (TC) that interacts with the midlatitude flow can cause large changes to the midlatitude flow pattern, it is much less understood if, and how, such events could impact a downstream tropical cyclone. Here, an indirect TC interaction is defined as one in which a primary TC perturbs the downstream midlatitude waveguide within one synoptic-scale wavelength of a secondary TC. In this study, a climatology and composite analysis using ERA-Interim reanalysis data is completed for all indirect interactions occurring between two tropical and/or subtropical cyclones in the North Atlantic and western North Pacific basins between 1989 and 2018. In all, 26 cases are identified in the North Atlantic and 56 cases are identified in the western North Pacific. The composite-mean interaction between a primary TC and upstream trough amplifies the immediate downstream ridge, increasing the tropospheric-deep vertical wind shear on its poleward and, in the western North Pacific, eastern, and equatorward flanks. An amplified downstream trough is detectable farther downstream in the western North Pacific 1–2 days after interaction onset; however, the same is not true in the North Atlantic, in which some cases exhibit anticyclonic Rossby wave breaking of the immediate downstream ridge. Secondary TCs that weaken following the indirect-interaction events are primarily located along the gradient between the downstream ridge and trough (North Atlantic) or at high latitudes (western North Pacific); those that strengthen are primarily located equatorward of the downstream ridge, particularly in the western North Pacific.

KEYWORDS: Synoptic climatology; Wave breaking; Extratropical cyclones; Tropical cyclones

1. Introduction

A significant fraction of tropical cyclones (TCs) recurve into the midlatitude flow in many tropical basins around the world, with approximately 37% of all western North Pacific TCs from 1979 to 2009 recurring (Archambault et al. 2013) and approximately 68% of North Atlantic TCs from 1950 to 2010 recurring (Colbert and Soden 2012). As these TCs recurve, their interaction with the midlatitude flow may cause increases in flow “waviness” (Archambault et al. 2013, 2015) and increased forecast errors downstream (Agustí-Panareda et al. 2004, 2005; McTaggart-Cowan et al. 2007; Harr and Dea 2009; Anwender et al. 2010; Grams et al. 2011, 2015; Pantillon et al. 2013; Riemer and Jones 2014; Keller et al. 2011, 2019). Extensive research has been published on the recurvature and extratropical transition (ET) of TCs (Jones et al. 2003; Evans et al. 2017; Keller et al. 2019) and the impact these recurring TCs have on the midlatitude waveguide (Anwender et al. 2008; Hedges et al. 2008;

Aiyer 2015; Grams and Archambault 2016; Keller et al. 2019; Pohorsky et al. 2019).

As a TC enters the midlatitudes, it may perturb the waveguide many thousands of kilometers downstream (Riemer and Jones 2010, 2014; Grams et al. 2013b; Keller 2017; Keller et al. 2019). This is accomplished primarily through the diabatically driven vertical redistribution of isentropic potential vorticity (PV) aloft, wherein PV is reduced (in the Northern Hemisphere) above the level of maximum diabatic warming near the TC’s center (Hoskins et al. 1985; Grams et al. 2011). This very-low PV air aloft is then advected radially outward, away from the TC’s center, by the TC’s divergent secondary circulation, tightening the local PV gradient and facilitating the creation of a jet or amplification of a preexisting jet (Riemer and Jones 2010; Grams et al. 2011, 2013a; Archambault et al. 2013, 2015; Grams and Archambault 2016). This jet strengthening, along with the poleward transport of warm, moist air, facilitates rapid ridge-building immediately downstream of the TC (Cunningham and Keyser 2000; Bosart 2003; Riemer and Jones 2010). The pattern reconfiguration associated

Corresponding author: Kevin Prince, kprince@uwm.edu

with the interaction between the midlatitude waveguide and primary TC may in some cases result in downstream anticyclonic wave breaking (Thorncroft et al. 1993; Zhang et al. 2017; Zhang and Wang 2018). Other factors that govern the extent to which a TC perturbs the midlatitude waveguide include characteristics of the midlatitude pattern itself, including but not limited to its antecedent wavelength and amplitude (Torn and Hakim 2015; Quinting and Jones 2016; Wirth et al. 2018; Finocchio and Doyle 2019), and the phasing of the TC with the upstream trough (e.g., Ritchie and Elsberry 2003, 2007; Scheck et al. 2011; Grams et al. 2013a; Archambault et al. 2013, 2015; Riemer and Jones 2014; Wirth et al. 2018; Komaromi and Doyle 2018; Keller et al. 2019; Riboldi et al. 2019).

A substantial portion of TCs form when one or more existing TCs are already present, with approximately one-third in the North Atlantic and nearly one-half in the western North Pacific forming with another TC already existing in its respective basin (Schenkel 2016, 2017). Furthermore, when two or more TCs are present within a given basin, the average distance between the TCs is approximately 1500 km in the North Atlantic and approximately 2000 km (approximately one synoptic-scale Rossby wavelength in each respective basin) in the western North Pacific (Schenkel 2017). While many studies have shown how midlatitude features can influence TC activity across a wide range of spatial and temporal scales (McTaggart-Cowan et al. 2007; Galarneau et al. 2015; Fowler and Galarneau 2017; Zhang et al. 2016, 2017), there has yet to be a *comprehensive* evaluation of TCs that perturb the midlatitude waveguide in the presence of a secondary TC and the impact this interaction can have on the secondary TC's track and intensity. Consequently, this study focuses on what is termed an *indirect* interaction (in contrast with the *direct* interaction first conceptualized by Fujiwhara 1921). Herein, an indirect interaction is conceptualized as the process of a primary TC influencing a secondary TC by influencing the synoptic-scale pattern in which the secondary TC is embedded.

A recent example of an indirect interaction is given by North Atlantic TCs Irma and Jose in 2017 (Fig. 1). As Irma recycles northward across the Florida peninsula, the TC interacts with an upstream shortwave trough over the southeastern United States. Negative PV advection by the primary TC's upper-tropospheric divergent outflow (as conceptualized by Archambault et al. 2013) tightens the local PV gradient between the TC and upstream trough, leading to local jet-streak enhancement and subsequent downstream ridge amplification (Fig. 1). Intensified upper-tropospheric northerly flow

on the eastern periphery of the Irma-amplified downstream ridge blocks Jose from propagating poleward and increases the vertical wind shear incident upon the TC. The increased vertical wind shear causes a rapid decrease in Jose's intensity from 115 kt (948 hPa) (1 kt \approx 0.5144 m s $^{-1}$) at 1200 UTC 10 September 2017 to 70 kt (979 hPa) at 1200 UTC 12 September 2017 (Berg 2018).

An example of multiple indirect interaction events in close temporal proximity occurred in 2010 between North Atlantic TCs Danielle, Earl, Fiona, and Gaston in 2010 (Fowler and Galarneau 2017). The recurvature of TC Danielle into a preexisting Rossby wave train over North America results in ridge amplification immediately downstream, which increases the meridional flow on its eastern and western flanks and, in turn, increases the vertical wind shear in proximity to three secondary TCs (Earl, Fiona, and Gaston). Forecast uncertainties associated with the initial interaction of TC Danielle with the midlatitude waveguide amplify downstream at medium-range lead times, reducing the midlatitude predictability across the North Atlantic and increasing forecast track errors for TCs Fiona and Gaston (Fowler and Galarneau 2017).

The purpose of this study is to produce a climatology of indirect TC interactions in the North Atlantic and western North Pacific basins from 1989 to 2018. This climatology provides a robust dataset for future studies to quantify the extent to which a primary TC can influence a secondary TC's track and intensity and more generally to document the influences of recurring TCs on the downstream tropical-to-subtropical environment across multiple basins. The improved understanding of these interactions is hoped to improve the understanding and predictability of the potential interaction outcomes, which may in turn lead to improved TC track and intensity forecasts. The paper is organized as follows. Datasets and analysis procedures are described in section 2. Section 3 details the indirect-interaction climatology, while section 4 documents the composite-mean tropospheric structure surrounding the time of the maximum interaction between the primary TC with the midlatitude flow. Section 5 discusses the impacts of the indirect-interaction events to primary and secondary TC track and intensity predictability. A summary and discussion are provided in section 6.

2. Methods

a. Data

The 6-hourly data from the European Centre for Medium-Range Weather Forecasts interim reanalysis dataset (ERA-Interim; Dee et al. 2011) are used to identify all indirect interactions. The dataset has roughly

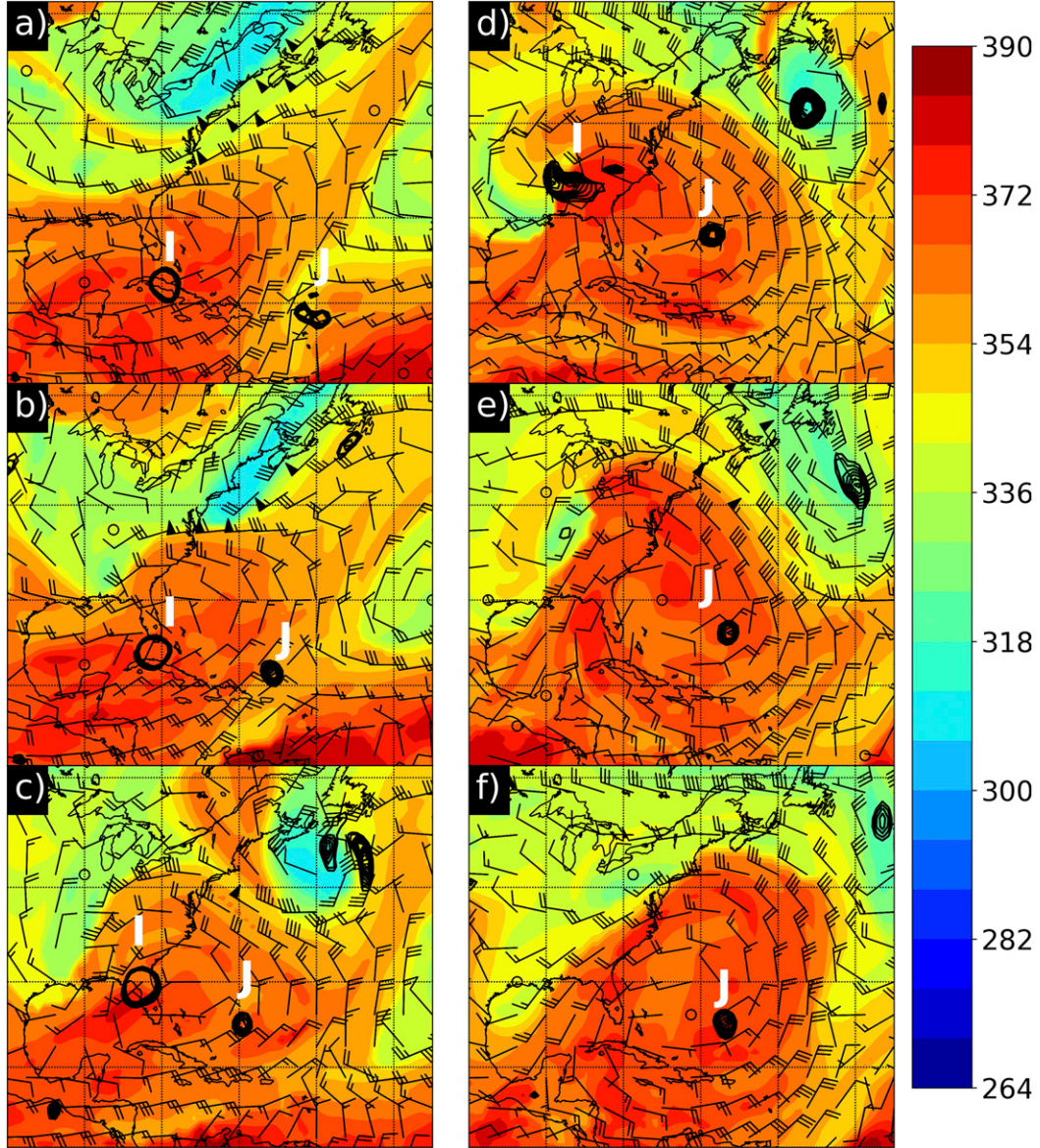


FIG. 1. Potential temperature (shaded in K per the color bar at right) on the 2 PVU (1 PVU = $10^{-6} \text{ K kg}^{-1} \text{ m}^2 \text{ s}^{-1}$) surface, horizontal wind on the 2 PVU surface (barbs; half-flag: 5 kt, flag: 10 kt, pennant: 50 kt), and 850 hPa relative vorticity (black contours; from 10 to $20 \times 10^{-5} \text{ s}^{-1}$ every 2 s^{-1}) at 1200 UTC (a) 9, (b) 10, (c) 11, (d) 12, (e) 13, and (f) 14 Sep 2017 for North Atlantic TCs Irma (primary; I) and Jose (downstream; J). Latitude and longitude lines are drawn every 10° .

80-km resolution on a reduced Gaussian grid with 60 isobaric levels up to 0.1 hPa. Best track and forecast track and intensity data for all TCs in the North Atlantic are collected from the NHC best track database (Landsea and Franklin 2013) and public archive (<ftp://ftp.nhc.noaa.gov/atcf/archive/>), respectively, while best track and forecast track and intensity data for the western North Pacific are collected from the Joint Typhoon Warning Center's collaboration site (JTWC 2019). Due to data availability limitations, note that the

forecast tracks in the western North Pacific are based only on TCs between 2002 and 2018.

b. Case selection

All classified tropical and subtropical cyclones, no matter their intensity, occurring in the North Atlantic and western North Pacific basins from 1989 to 2018 are considered as potential cases. While classification practices for the North Atlantic do change somewhat during this time frame, these have been shown to have a

minimal impact on total TC counts per year, resulting in minimal impacts to the number of indirect interactions (Landsea 2007). The same period was selected for the western North Pacific for consistency.

Two screening steps are followed to identify indirect-interaction events. The first filtering step requires that two or more TCs concurrently exist for all candidate events. As a TC interacts with an upstream trough, the resulting perturbation is most pronounced within one wavelength downstream (Riemer and Jones 2010, 2014; Grams et al. 2013b; Keller 2017; Keller et al. 2019; Pohorsky et al. 2019). Therefore, the second screening step requires that the two TCs be within this distance, as determined by the geometry of the midlatitude flow at the time of interaction. Note that a TC may both be influenced by and subsequently influence an additional secondary TC, which is counted as two interaction events. However, a TC that influences more than one secondary TC (although there are no such cases within the dataset considered due to the one-wavelength restriction) is a single interaction event.

The Archambault et al. (2013) interaction metric is used to ensure that the midlatitude-flow reconfiguration downstream of a candidate primary TC is at least partially the result of the primary TC's diabatically driven upper-tropospheric divergent outflow impinging upon the midlatitude waveguide. The interaction metric is defined as the negative PV advection by the divergent (or irrotational) component of the wind:

$$-\mathbf{V}_x \cdot \nabla_p PV < 0, \quad (1)$$

where \mathbf{V}_x is the 250–150 hPa-averaged irrotational component of the horizontal wind and $\nabla_p PV$ is the 250–150 hPa-averaged PV gradient. Candidate events must be associated with an instantaneous metric value of -1 PVU day^{-1} or lower at one or more locations within 500 km of the primary TC's center, consistent with Archambault et al. (2013, 2015; albeit with a coarser dataset in their study), to be included. Compositing (section 2c) is temporally centered on the *time of maximum interaction*, defined as the time at which the interaction metric achieves its maximum magnitude.

In contrast to the indirect interaction between TCs Irma and Jose depicted in Fig. 1, not all TC pairs for which a primary TC recycles into the midlatitudes and undergoes ET qualify as indirect-interaction events. A representative example is given by North Atlantic TC Ophelia in 2011, which recurved into the midlatitude flow while TC Philippe began to develop to its southeast (Fig. 2). As Ophelia recycles into the midlatitude flow, an area of negative PV advection more negative than the -1 PVU day^{-1} threshold is present but is located

1500–2000 km west of TC Ophelia (Fig. 2f). A closer inspection reveals that a majority of Ophelia's upper-tropospheric outflow is directed eastward into the midlatitude ridge rather than westward against the trough (Figs. 2f,g), such that the negative PV advection to Ophelia's west results from other forcings (e.g., deep, moist convection along the U.S. East Coast) rather than from Ophelia. Further, the direction of TC Ophelia's outflow primarily into the midlatitude ridge to its east cannot result in significant midlatitude amplification, and thus no indirect interaction with TC Philippe, as the Petterssen development parameters (upper-tropospheric divergence, lower-tropospheric warm-air advection, and midtropospheric cyclonic vorticity advection) indicate that only immediately ahead of a trough is significant amplification to the midlatitude waveguide by a TC possible (Petterssen and Smebye 1971; Keller et al. 2019).

c. Compositing

Two compositing approaches are used in this study, one to document the impact the primary TCs have on the midlatitude waveguide downstream of their maximum interaction location and one to document differences in the large-scale environments between secondary TCs that weaken or intensify in the 48 h following the time of maximum interaction. The first approach composites around the fixed spatial location of the maximum absolute value of negative PV advection by the irrotational wind at the time of maximum interaction between the primary TC and the midlatitude waveguide (as in Archambault et al. 2015). The second approach is spatially centered on the (temporally variable) secondary TCs' locations. Both approaches use a domain encompassing $\pm 37.5^\circ$ latitude and 45° longitude west to 90° longitude east of their respective centering points and are generated for a 96-h period between 48 h prior to and 48 h after the time of maximum interaction of the primary TC with the midlatitude waveguide.

d. Ventilation index calculation

The ventilation index of Tang and Emanuel (2012) is used to better understand the tropospheric-deep impacts of indirect-interaction events to the environments within which the secondary TCs are embedded. This index is defined as

$$\Lambda = \frac{u_{\text{shear}} \chi_m}{u_{\text{PI}}}, \quad (2)$$

where $u_{\text{shear}} = |\mathbf{v}_{850} - \mathbf{v}_{200}|$ is the bulk environmental vertical wind shear magnitude between 850 and 200 hPa, u_{PI} is the maximum potential intensity (MPI), and χ_m is

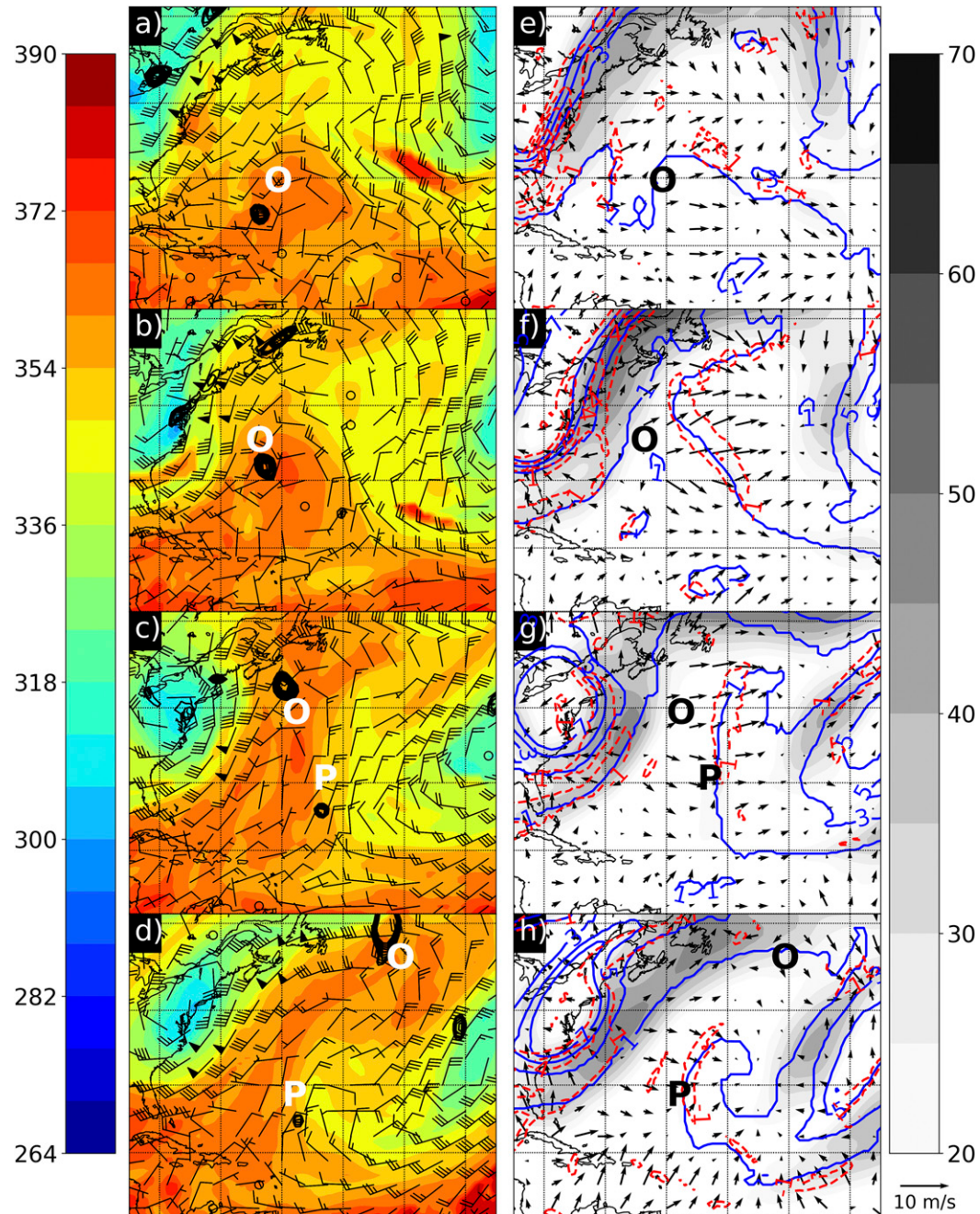


FIG. 2. (a)–(d) Potential temperature (shaded in K per the color bar at left) on the 2 PVU surface, horizontal wind on the 2 PVU surface (barbs; half-flag: 5 kt, flag: 10 kt, pennant: 50 kt), and 850 hPa relative vorticity (black contours; from 10 to $20 \times 10^{-5} \text{ s}^{-1}$ every 2 s^{-1}) at 0000 UTC (a) 1, (b) 2, (c) 3, and (d) 4 Oct 2011 for North Atlantic TCs Ophelia (primary; O) and Philippe (downstream; P). (e)–(h) The 250–150 hPa layer-mean PV (blue contours every 2 PVU starting at 1 PVU), 250–150 hPa layer-mean horizontal wind speed (shaded in m s^{-1} per the color bar at right), 250–150 hPa layer-mean irrotational wind (vectors; m s^{-1} ; reference vector at lower right), and 250–150 hPa advection of the layer-mean potential vorticity by the layer-mean irrotational wind (red-dashed contours every -3 PVU day^{-1} starting at -1 PVU day^{-1}) at the same times as in (a)–(d). Latitude and longitude grid lines are drawn every 10° .

TABLE 1. Climatological information on all 26 primary and secondary TCs in the North Atlantic basin, as sorted in decreasing order based on the magnitude of the temporally (from 48 h before the time of maximum interaction to 48 h after) and spatially (over a box extending 7.5° in all directions from the location of maximum interaction) averaged value of the interaction metric, as defined by Archambault et al. (2013).

Primary TC storm name	Secondary TC storm name	Date of max interaction	Interaction metric (PVU day^{-1})
Florence (2006)	Gordon (2006)	0600 UTC 11 Sep	-2.87
Floyd (1999)	Gert (1999)	0000 UTC 16 Sep	-2.20
Ivan (2004)	Jeanne (2004)	1800 UTC 8 Sep	-1.88
Matthew (2016)	Nicole (2016)	1800 UTC 8 Oct	-1.72
Irene (2011)	Jose (2011)	0600 UTC 28 Aug	-1.60
Jeanne (2004)	Karl (2004)	1200 UTC 17 Sep	-1.58
Odette (2003)	Peter (2003)	0000 UTC 8 Dec	-1.42
Igor (2010)	Julia (2010)	0600 UTC 19 Sep	-1.41
Irma (2017)	Jose (2017)	1800 UTC 10 Sep	-1.29
Gabrielle (2001)	Felix (2001)	1800 UTC 14 Sep	-1.27
Karl (2016)	Lisa (2016)	0000 UTC 25 Sep	-1.24
Fabian (2003)	Isabel (2003)	1200 UTC 7 Sep	-1.22
Karl (2004)	Lisa (2004)	0000 UTC 21 Sep	-0.92
Gordon (2000)	Helene (2000)	1800 UTC 16 Sep	-0.79
Isidore (2002)	Kyle (2002)	0600 UTC 25 Sep	-0.79
Michael (2000)	Nadine (2000)	1200 UTC 19 Oct	-0.76
Maria (2005)	Nate (2005)	0000 UTC 24 Sep	-0.73
Fran (1996)	Hortense (1996)	1800 UTC 30 Aug	-0.60
Hanna (2008)	Ike (2008)	1800 UTC 3 Sep	-0.56
Karl (1998)	Jeanne (1998)	1800 UTC 26 Sep	-0.55
Katrina (2005)	Lee (2005)	1800 UTC 30 Aug	-0.52
Earl (2010)	Fiona (2010)	1800 UTC 31 Aug	-0.52
Danielle (2010)	Earl (2010)	1200 UTC 29 Aug	-0.49
Isabel (2003)	Juan (2003)	1800 UTC 17 Sep	-0.34
Gustav (2008)	Hanna (2008)	1200 UTC 31 Aug	-0.30
Gustav (1990)	Hortense (1990)	1800 UTC 1 Sep	-0.10

the nondimensional entropy deficit. The entropy deficit χ_m is defined as

$$\chi_m = \frac{s_m^* - s_m}{s_{\text{SST}}^* - s_b}, \quad (3)$$

where s_m^* is the saturation entropy at 600 hPa in the TC's inner core, s_m is the environmental entropy at 600 hPa, s_{SST}^* is the saturation entropy at the sea surface temperature (SST), and s_b is the entropy of the boundary layer. The derivation of the ventilation index and details of calculating the ventilation index from gridded data can be found in Tang and Emanuel (2012). Due to the coarseness of the ERA-Interim SST data, the SST data are substituted with daily optimum-interpolation 0.25°SST data (Reynolds et al. 2007; Banzon et al. 2016) for the calculations of the entropy deficit and MPI to better represent spatiotemporal SST variability; however, qualitatively identical results are obtained when instead using the ERA-Interim SSTs (not shown).

e. Forecast error calculation

To quantify the track/intensity predictability for the primary and secondary TCs, official warning-center

(NHC for the North Atlantic, Joint Typhoon Warning Center for the western North Pacific) track and intensity forecasts are verified. Errors are calculated following NHC operational practice, such that only TCs that attain tropical-storm or hurricane/typhoon status are included in the evaluation. Additionally, forecasts that verify over land are included, but forecasts verifying after the TC is no longer classified as tropical are excluded. Forecast errors for both primary and secondary TCs are computed at multiple forecast lead times surrounding the time of maximum interaction; however, the analysis presented herein focuses only on forecasts issued between 24 and 48 h before the time of maximum interaction. This time corresponds with the times at which the basin-wide predictability at medium-ranges (e.g., 2–5+ days) is typically degraded due to the uncertainty in predicting the interaction of the primary TC with the upstream trough (Aiyer 2015; Harr and Archambault 2016).

f. Statistical-significance testing

The extent to which composite-mean atmospheric fields (sections 2c and 2d) and official-forecast track and intensity errors (section 2e) are significantly different

TABLE 2. As in Table 1, but for the 56 cases in the western North Pacific basin.

Primary TC storm name	Secondary TC storm name	Date of max interaction	Interaction metric (PVU day ⁻¹)
Lan (2017)	Saola (2017)	1200 UTC 21 Oct	-3.69
Soulik (2006)	Rumbia (2006)	0000 UTC 6 Oct	-3.56
Songda (2004)	Sarika (2004)	0600 UTC 7 Sep	-3.54
Wipha (2013)	Francisco (2013)	1200 UTC 15 Oct	-3.47
Talas (2011)	Noru (2011)	1200 UTC 2 Sep	-3.20
Megi (2004)	Aere (2004)	0600 UTC 18 Aug	-3.16
Podul (2001)	Ling-Ling (2001)	1200 UTC 26 Oct	-3.12
Fitow (2013)	Danas (2013)	0600 UTC 4 Oct	-3.07
Melor (2009)	Nepartak (2009)	0000 UTC 7 Oct	-2.90
Zeb (1998)	Babs (1998)	0000 UTC 17 Oct	-2.70
Tokage (2004)	Nock-Ten (2004)	1200 UTC 20 Oct	-2.58
Francisco (2013)	Lekima (2013)	1800 UTC 24 Oct	-2.46
Saomai (2000)	Sonamu (2000)	0000 UTC 15 Sep	-2.46
Jelawat (2012)	Ewiniar (2012)	0600 UTC 29 Sep	-2.44
Bolaven (2012)	Tembin (2012)	0600 UTC 28 Aug	-2.38
Lupit (2009)	Mirinae (2009)	1800 UTC 26 Oct	-2.26
Kompasu (2010)	Malou (2010)	1800 UTC 1 Sep	-2.26
Chaba (2010)	Seventeen (2010)	0600 UTC 30 Oct	-2.23
Rusa (2002)	Sinlaku (2002)	1800 UTC 31 Aug	-2.21
Ketsana (2003)	Parma (2003)	0600 UTC 25 Oct	-2.19
Ryan (1992)	Sibyl (1992)	1800 UTC 10 Sep	-2.18
Dianmu (2004)	Mindulle (2004)	0600 UTC 21 Jun	-2.13
Fitow (2007)	Danas (2007)	1800 UTC 7 Sep	-2.06
Haiyan (2001)	Podul (2001)	1800 UTC 17 Oct	-2.06
Chan-Hom (2015)	Nangka (2015)	0000 UTC 12 Jul	-2.02
David (1997)	Ella (1997)	1200 UTC 16 Sep	-2.01
Goni (2015)	Atsani (2015)	0600 UTC 25 Aug	-1.92
Aere (2004)	Chaba (2004)	1800 UTC 30 Aug	-1.91
Nida (2004)	Omais (2004)	0600 UTC 20 May	-1.91
Zane (1996)	Yates (1996)	0600 UTC 29 Sep	-1.87
Chanthu (2016)	Mindulle (2016)	0000 UTC 17 Aug	-1.87
Rammasun (2002)	Chataan (2002)	0600 UTC 5 Jul	-1.85
Robyn (1993)	Steve (1993)	0000 UTC 10 Aug	-1.78
Mawar (2005)	Guchol (2005)	0000 UTC 25 Aug	-1.63
Prapiroon (2012)	Maria (2012)	0600 UTC 18 Oct	-1.57
Chataan (2002)	Halong (2002)	1800 UTC 10 Jul	-1.57
Shanshan (2006)	Yagi (2006)	1800 UTC 17 Sep	-1.56
Kong-Rey (2013)	Toraji (2013)	0000 UTC 31 Aug	-1.45
Fung-Wong (2014)	Kalmaegi (2014)	1800 UTC 23 Sep	-1.34
Prapiroon (2000)	Saomai (2000)	0600 UTC 31 Aug	-1.31
Mindulle (2004)	Ting-Ting (2004)	0600 UTC 4 Jul	-1.10
Page (1990)	Owen (1990)	0000 UTC 29 Nov	-1.09
Roger (1989)	Sarah (1989)	0600 UTC 26 Aug	-1.07
Omar (1992)	Polly (1992)	1200 UTC 31 Aug	-1.04
Sinlaku (2008)	Sixteen (2008)	0600 UTC 10 Sep	-0.96
Pabuk (2001)	Wutip (2001)	0000 UTC 21 Aug	-0.92
Kong-Rey (2018)	Trami (2018)	0600 UTC 30 Sep	-0.91
Orchid (1994)	Ruth (1994)	1200 UTC 26 Sep	-0.82
Olga (1999)	Paul (1999)	0000 UTC 3 Aug	-0.82
Muifa (2011)	Merbok (2011)	1200 UTC 7 Aug	-0.74
Violet (1996)	Tom (1996)	0000 UTC 17 Sep	-0.53
Walt (1994)	Zeke (1994)	0600 UTC 20 Jul	-0.49
Rosie (1997)	Scott (1997)	0600 UTC 25 Jul	-0.47
Damrey (2012)	Haikui (2012)	0600 UTC 30 Jul	-0.42
Rumbia (2018)	Soulik (2018)	0600 UTC 16 Aug	-0.41
Morakot (2009)	Etau (2009)	0600 UTC 9 Aug	-0.34

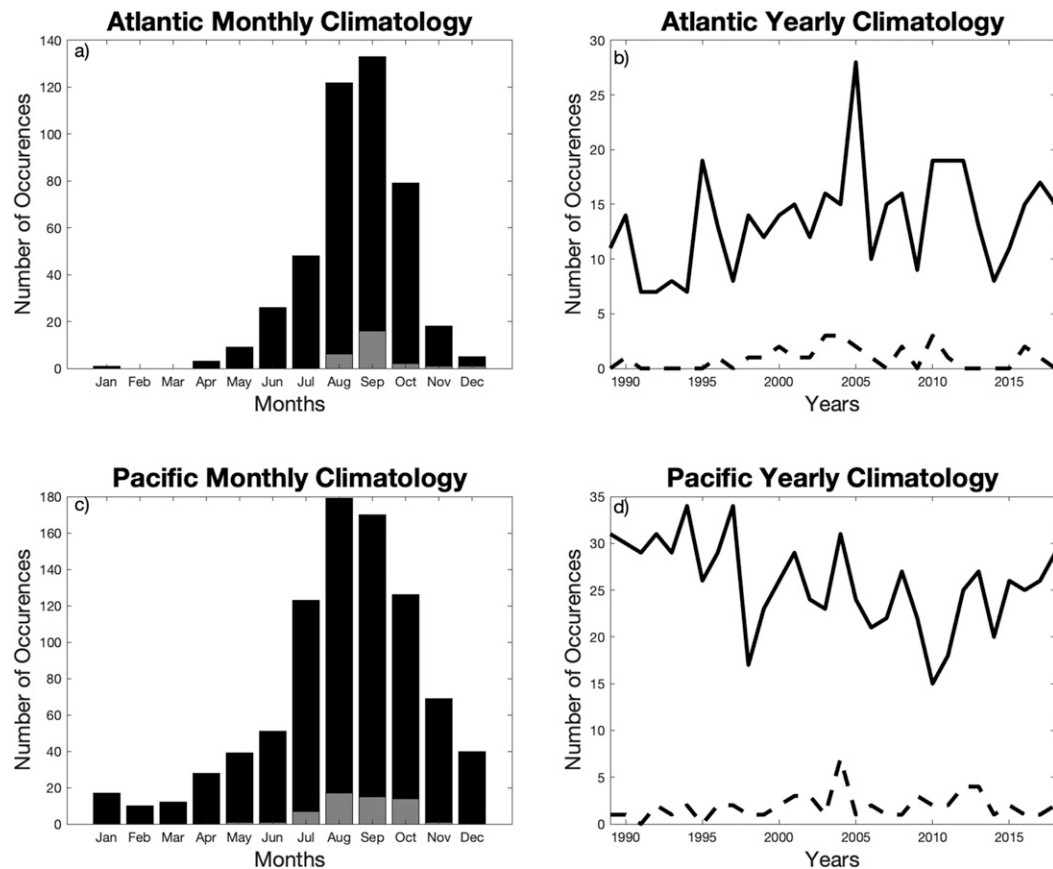


FIG. 3. Indirect-interaction occurrence (light gray bar; dashed line) compared to the total number of TCs (black bar; solid line) as a function of month aggregated (a) over all years, and (b) yearly for the North Atlantic. (c),(d) As in (a),(b), but for the western North Pacific.

from climatology is assessed using Monte Carlo bootstrapping (Efron and Tibshirani 1994).

For composite-mean atmospheric fields, the climatology is defined using a 15-day average centered on the date of each indirect-interaction event (the time of maximum interaction) over the period 1980–2010, with this 30-yr duration selected following current operational practices for defining climate normals. Next, 1000 samples of anomalies (each with a sample size equal to the number of indirect-interaction events in each basin) are randomly drawn from dates in 1980–2010 between one week prior to one week after the date of each indirect-interaction event, with each event contributing one member per sample. Composite-mean atmospheric fields are said to be significantly different from climatology to 95% confidence when they are smaller than the 25th-ranked or larger than the 975th-ranked samples of climatological anomalies.

For official forecasts, the climatology is defined from the set of all TCs (separately for the North Atlantic and western North Pacific basins) between 1989 and 2018

excluding the primary and secondary TCs. Additionally, these official forecasts include forecasts that verify over land, but forecasts verifying after the TC is no longer classified as tropical are excluded. Next, 10 000 samples of forecast errors (each with a sample size equal to the number of indirect-interaction events in each basin) are randomly drawn from climatology, with separate samples drawn at each forecast lead time considered (0, 12, 24, 36, 48, 72, 96, and 120 h). Composite-mean forecast errors are said to be significantly different from climatology to 95% confidence when they are smaller than the 250th-ranked or larger than the 9750th-ranked samples of climatological mean forecast errors.

3. Event climatology

A total of 26 indirect interactions are identified for the North Atlantic basin (Table 1), whereas 56 are identified for the western North Pacific basin (Table 2). It is speculated that the greater number of events for the western North Pacific largely results from the higher

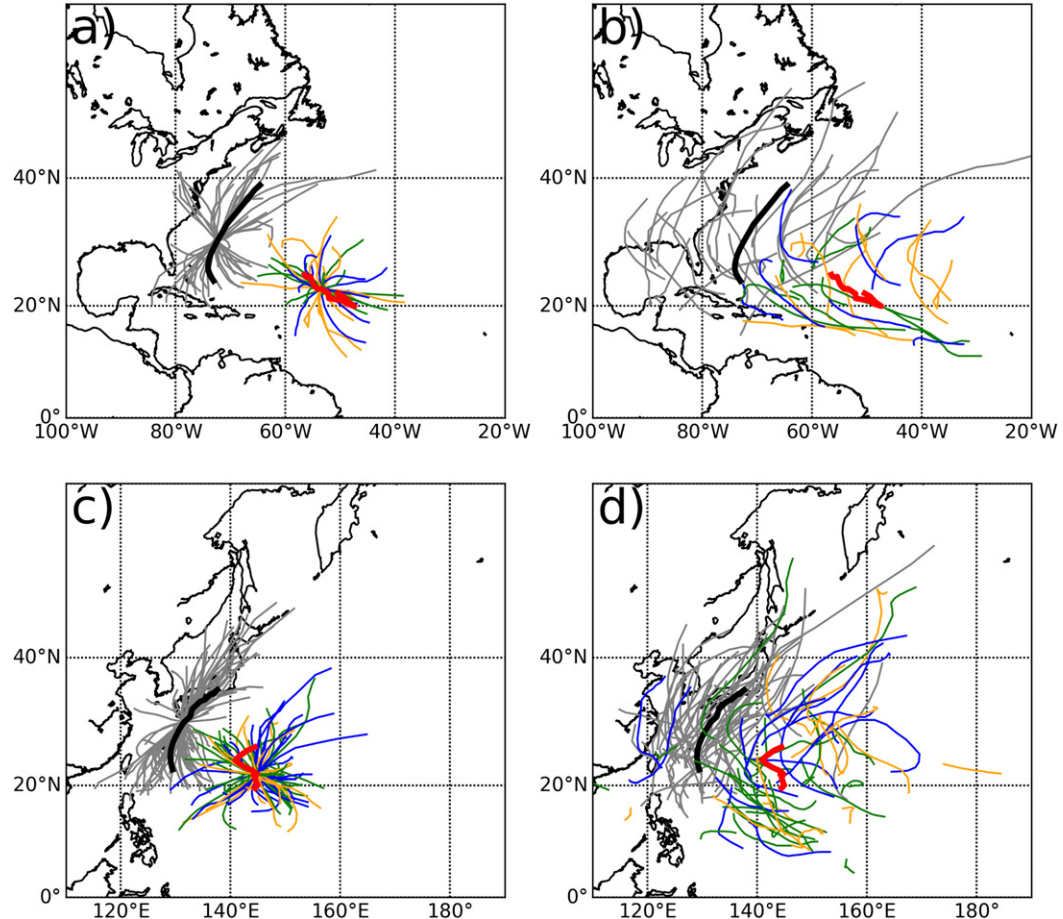


FIG. 4. Best track TC tracks for all indirect-interaction primary TCs (as given by the thin gray lines) in the (a),(b) North Atlantic and (c),(d) western North Pacific basins from 48 h before the time of maximum interaction to 48 h after at 6-h increments. (a),(c) Tracks shifted to the average primary-TC location at the time of maximum interaction, whereas (b),(d) unshifted TC tracks. The thick black lines depict the average primary-TC tracks over the 96-h period considered, whereas the thick red lines depict the average secondary-TC tracks over the 96-h period considered. Orange lines represent the tracks of secondary TCs that did not change intensity (again utilizing minimum central pressure to define these criteria as in Tables 3 and 4), blue lines represent the tracks of secondary TCs that weakened over the 48 h after the time of maximum interaction, and green lines represent the tracks of secondary TCs that strengthened over the 48 h after the time of maximum interaction.

number of TCs in this basin (approximately 24 TCs per year over the 30-yr climatology; JTWC 2018) as compared to the North Atlantic basin (approximately 15 TCs per year over the 30-yr climatology; Landsea and Franklin 2013). Unsurprisingly, the months in which TCs typically form are also the months with the highest numbers of indirect interaction events, with an extremely high linear-correlation coefficient (0.79 with a p value of 0.11 for the North Atlantic; 0.95 with a p value of 10^{-4} for the western North Pacific; note that this and subsequent p values in this subsection are assessed using a Student's t test excluding all occurrences of zero for both values) between the monthly climatologies for both basins (Fig. 3). Further, the *annual* counts of TCs and indirect interaction events in a given basin are

moderately linearly correlated (0.35 with a p value of 0.18 for the North Atlantic; 0.21 with a p value of 0.28 for the western North Pacific; see also Figs. 3b and 3d).

The indirect interactions identified herein are associated with highly variable tracks for both the primary and secondary TCs (Fig. 4) and correspondingly variable midlatitude flow configurations (Fig. 5). Even when centered around a common location, here given by the average location of the primary TCs at the time of maximum interaction, there is still significant track variability away from the time of maximum interaction (Figs. 4a,c) that is most pronounced in the North Atlantic (Fig. 4a). A shorter composite track for secondary TCs in both basins is representative of a slower translation speed for these TCs than their primary counterparts because the

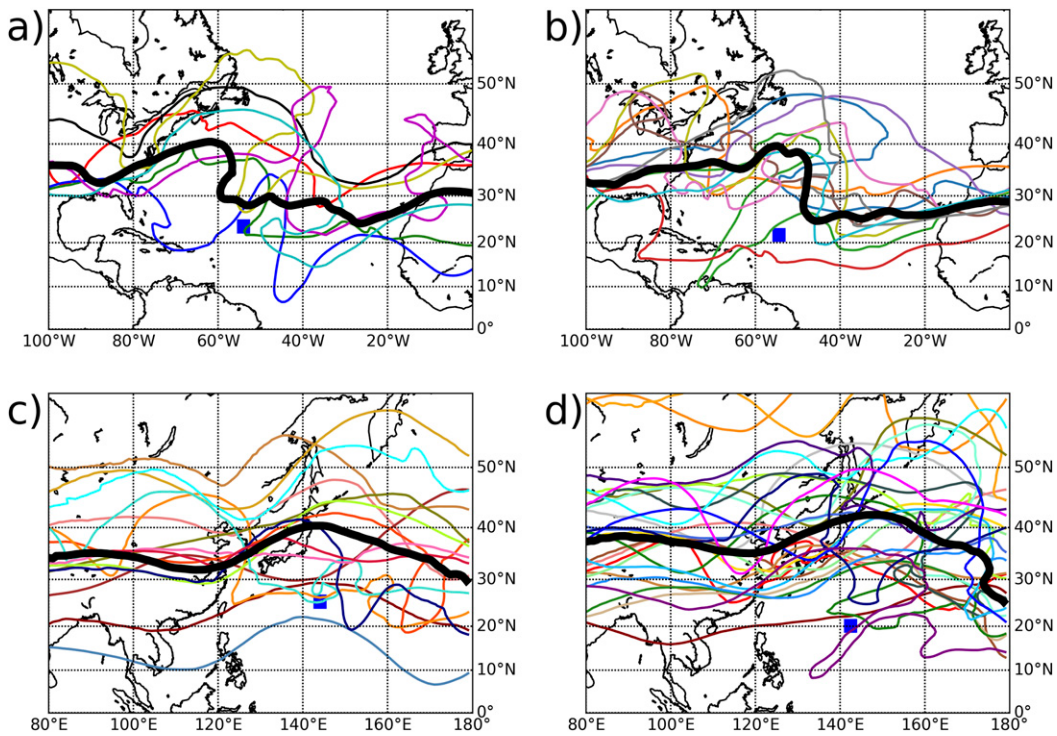


FIG. 5. Analysis of the 2-PVU contour on the 340 K isentropic surface (taken as a proxy for the midlatitude waveguide) averaged from 48 h before the time of maximum interaction to 48 h after the time of maximum interaction for (a) the 7 weakening North Atlantic, (b) the 10 strengthening North Atlantic, (c) the 15 weakening western North Pacific, and (d) the 28 strengthening western North Pacific secondary TCs. Each individual waveguide is shown with different colored skinny lines, whereas the composite-mean waveguide for each subset is shown by the bold black contour. The average location of the secondary TCs over the 96-h period from 48 h before the time of maximum interaction to 48 h after the time of maximum interaction is given by the blue square.

primary TCs are at higher latitudes where large-scale tropospheric-deep flow is typically stronger (Fig. 4). In the North Atlantic weakening secondary TCs are slightly farther north and east than their strengthening or no-

change counterparts (Figs. 4a,b and Table 3), whereas weakening secondary TCs in the western North Pacific are farther north and slightly east of nonweakening secondary TCs (Figs. 4c,d and Table 4).

TABLE 3. Selected parameters for the secondary TCs in the North Atlantic basin, separated by whether the secondary TCs strengthened, weakened, or did not change intensity. A change in central pressure of less than 5 hPa over the 96-h period from 48 h before the time of maximum interaction to 48 h after following the indirect-interaction event classified a TC as no change, an increase of 5 hPa or greater as weakening, and a decrease of 5 hPa or greater as strengthening. The average time in the life cycle is represented by a 0 for the beginning of the TC's life and a 1 for the ending. MPI is calculated following the calculation in Tang and Emanuel (2012) over a 5° by 5° moving domain located 48 h ahead of each secondary TC along its track to attain the environmental MPI (i.e., that uninfluenced by the TC). Vertical wind shear magnitude is calculated over a 5° by 5° moving domain following each secondary TC with the secondary TC's circulation removed using vorticity inversion.

Count	Strengthening	Weakening	No change
	10	7	9
Avg normalized time in life (1 = last advisory, 0 = first advisory)	0.23	0.41	0.44
Avg normalized intensity relative to MPI (1 = at MPI, 0 = 0 kt)	0.25	0.67	0.21
Avg min sea level pressure change (hPa)	-22.8	12.6	-0.67
Avg 850–200 hPa vertical wind shear magnitude (in m s^{-1})	4.96	6.68	5.83
Average change in 850–200 hPa vertical wind shear magnitude (in m s^{-1})	2.08	-1.59	0.58
Avg lat	21.8°N	23.6°N	23.7°N
Avg lon	-54.5°W	-54°W	-50.4°W
Avg great-circle distance from waveguide (km)	607.7	440.8	450

TABLE 4. As in Table 3, but for the 56 cases in the western North Pacific basin.

Count	Strengthening	Weakening	No change
	28	15	13
Avg normalized time in life (1 = last advisory, 0 = first advisory)	0.30	0.66	0.39
Avg normalized intensity relative to MPI (1 = at MPI, 0 = 0 kt)	0.24	0.74	0.30
Avg min sea level pressure change (hPa)	-20.8	23.3	-0.6
Avg 850–200 hPa vertical wind shear magnitude (m s^{-1})	2.62	5.22	4.28
Avg change in 850–200 hPa vertical wind shear magnitude (m s^{-1})	0.02	4.21	1.11
Avg lat	19.9°N	25.4°N	24.2°N
Avg lon	142.3°E	144°E	152°E
Avg great-circle distance from waveguide (km)	986.5	826.3	911.5

Changes in the secondary TCs' translation speed and intensity during and after the indirect-interaction event are small on average but highly variable between cases. For instance, there is little change in average translation speed occurring after the time of maximum interaction for the secondary TCs (Figs. 6c,d). There are also minimal impacts to intensity (in terms

of maximum wind speed) for the secondary TCs, with a 7-kt mean increase in intensity for the North Atlantic (Fig. 6a) and 6-kt mean increase for the western North Pacific (Fig. 6b) over the period from the time of maximum interaction to 48 h after. However, there is substantial case-to-case variability in intensity and translation speed before, during, and after the

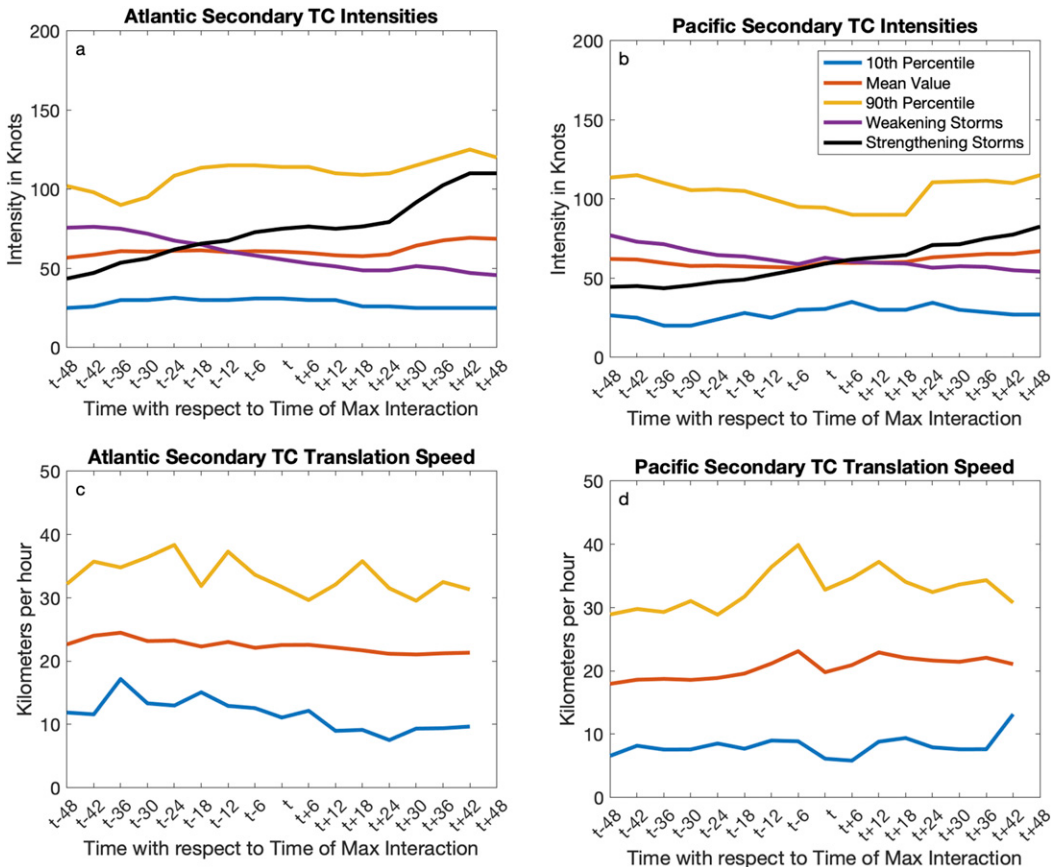


FIG. 6. Secondary TC (a),(b) intensity (kt) and (c),(d) translation speeds (km h^{-1}) for the (a),(c) North Atlantic and (b),(d) western North Pacific (right column) basins. The blue line represents the 10th percentile of the dataset, the red line represents the mean, and the orange line represents the 90th percentile. All fields are shown at 6-h increments from 48 h prior to through 48 h after the time of maximum interaction between the primary TCs and the midlatitude waveguide. The weakening (purple line) and strengthening (black line) subsets in (a) and (b) are the same as those identified in Tables 3 and 4.

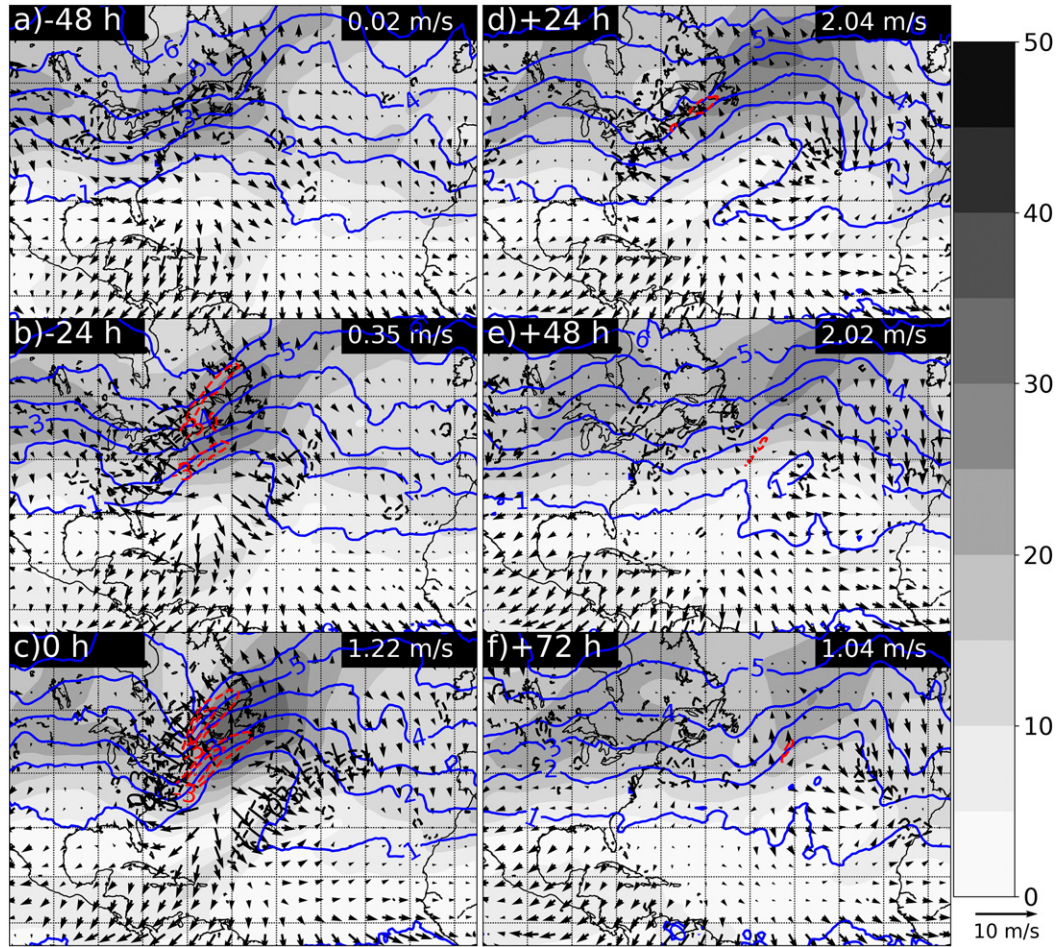


FIG. 7. Maximum-interaction-centered composite-mean 250–150 hPa layer-mean PV (blue contours every 1 PVU starting at 1 PVU), 250–150 hPa layer-mean horizontal wind speed (gray shading in m s^{-1} per the color bar at right), 250–150 hPa layer-mean irrotational wind (vectors in m s^{-1} ; reference vector at lower right), 250–150 hPa layer-mean PV advection by the layer-mean irrotational wind (red-dashed contours every -3 PVU day^{-1} starting at -3 PVU day^{-1}), and 250–150 hPa layer-mean divergence (black-dashed contours every $-0.3 \times 10^{-5} \text{ s}^{-1}$ starting at 0 s^{-1}) every 24 h from (a) 48 h before the time of maximum interaction to (h) 120 h after the time of maximum interaction for the North Atlantic basin ($n = 26$). Latitude and longitude grid lines are drawn every 10° . Meridional-flow index anomalies [defined as in Archambault et al. (2013) relative to a 1980–2010 monthly mean climatology between 20° – 50°N and 80° – 20°W ; units: m s^{-1}] are plotted in white text in the top-right corner of each panel. Note that spatial composites are centered on the composite-mean location of the maximum interaction, such that the geography highlighted on the map is for spatial reference only.

indirect-interaction event, as shown by the large differences between the strengthening and weakening cases in both basins (Figs. 6a,b). These findings are consistent with Peirano et al. (2016) and Fischer et al. (2017), as those studies highlighted significant distinctions in terms of how TC intensity changes as it encounters a trough, with these differences being largely tied to the flow geometry associated with the upstream trough and suggest the need for case-to-case diagnosis.

With an average separation distance between the primary and secondary TCs of 2065 km in the North Atlantic and 1630 km in the western North Pacific at the

time of maximum interaction, the primary and second TCs are sufficiently distant from each other for any potential influence of the primary TC on the secondary TC to largely be indirect rather than direct. For instance, although upwelling locally reduces SST along the primary TCs' paths (section 4a), a majority of secondary TCs follow a track sufficiently distant from those of their predecessor primary TCs to not be significantly impacted by this upwelling and its associated atmospheric impacts (not shown). Further, the separation between the primary and secondary TCs exceeds the ~ 1500 km maximum separation distance required for mutual

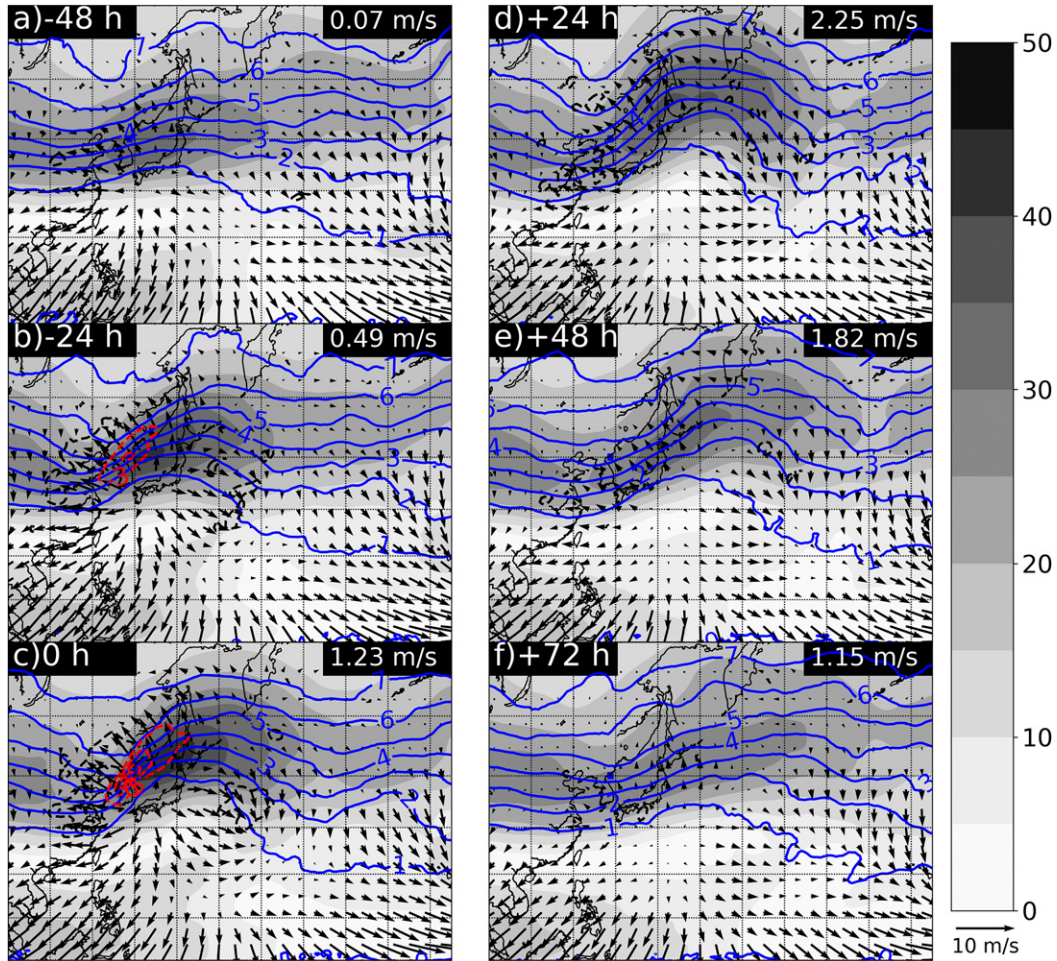


FIG. 8. As in Fig. 7, but for the western North Pacific basin ($n = 56$). The spatial bounds for the meridional-flow index anomalies in this figure are 20° – 50° N, 140° E– 120° W.

rotation of each TC about the other to occur (Fujiwhara 1921). However, the primary TCs are sufficiently close to their respective secondary TCs to impart a weak steering current (in the composite mean) across the secondary TCs. Inverting the 850–200 hPa layer-mean relative vorticity within 4.5° of the primary TCs' center (following Galarneau and Davis 2013 and Papin 2017) at the time of maximum interaction results in a 850–200 hPa layer- and composite-mean nondivergent wind of 0.57 m s^{-1} in the North Atlantic and 0.71 m s^{-1} in the western North Pacific across the secondary TCs, albeit with significant variability between cases (standard deviation of 0.57 m s^{-1} in the North Atlantic, 0.77 m s^{-1} in the western North Pacific).

4. Synoptic composites

Two compositing approaches are used to document the large-scale flow reconfiguration associated

with the indirect-interaction events described in the previous section. The first, a maximum-interaction-centered approach (section 4a), is used to identify the composite-mean impacts of the primary TCs' interaction with the midlatitude waveguide on downstream subtropical to midlatitude pattern (section 4a). The second, a secondary-TC-centered approach (section 4b), is used to document variability in the reconfigured large-scale pattern between secondary TCs that strengthen and weaken during indirect-interaction events.

a. Composite-mean impacts of primary TCs on their synoptic-scale environments and the midlatitude waveguide

The onset of an indirect-interaction event, occurring between 48 and 24 h prior to the time of maximum interaction in each basin, is characterized by large composite-mean negative PV advection by the irrotational wind resulting from the composite-mean

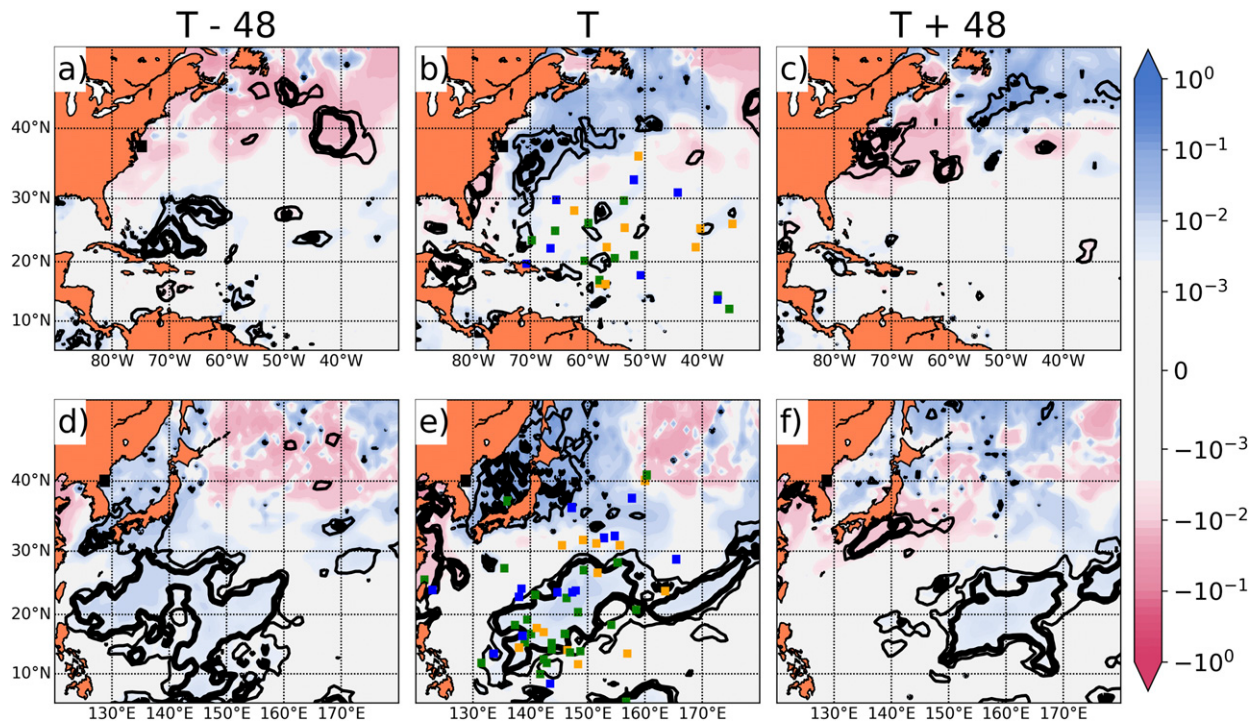


FIG. 9. Maximum-interaction-centered composite-mean ventilation index anomaly (shaded per the logarithmic color bar at right; blue shading represents higher ventilation index values and a less conducive environment to TC formation and maintenance and red shading represents lower values more supportive of TC formation and maintenance) every 48 h from (a),(d) 48 h before the time of maximum interaction to (c),(f) 48 h after the time of maximum interaction. The thin black line denotes anomalies that are statistically significant to at least 95% confidence and the thick black line denotes anomalies that are statistically significant to at least 99% confidence. (a)–(c) The North Atlantic composite and (d)–(f) the western North Pacific composite. Black squares in each panel indicate the composite-mean location of maximum interaction. Orange squares in (b) and (e) indicate the shifted locations of the secondary TCs (relative to the composite-mean primary TC location) at the time of maximum interaction for all TCs that did not change in intensity from 48 h before the time of maximum interaction to 48 h after, blue squares indicate the shifted locations of the secondary TCs that weakened, and green squares indicate the shifted locations of secondary TCs that strengthened.

upper-tropospheric outflow associated with the composite-mean primary TCs impinging upon the antecedent midlatitude waveguide (Figs. 7 and 8a,b). Concurrently, the ventilation index is anomalously high to the south-southeast of the composite-mean location of maximum interaction in both basins (Figs. 9a,d); however, this primarily reflects the direct influence of the composite-mean primary TCs on their immediate environments. The anomalously high ventilation index values largely result from anomalously weak composite-mean MPI (Figs. 10a,d), anomalously high composite-mean entropy deficit (Figs. 11a,d) and, to lesser extent, anomalously high composite-mean 850–200 hPa vertical wind shear (Figs. 12a,d). Upwelling induced by the primary TCs is the cause of the anomalously weak MPI and anomalously large entropy deficit (not shown; Hart et al. 2007; Schenkel and Hart 2015). The areas of statistical significance are larger in spatial extent for the western North Pacific than for the North Atlantic, which is hypothesized to be due to the

smaller spread of primary TC locations (and thus greater local impact that rises to the level of statistical significance) in the western North Pacific (Fig. 4).

By the time of maximum interaction, the primary TC has already been interacting with the midlatitude waveguide for approximately 1–2 days. Over these 1–2 days, a tightening of the horizontal PV gradient between the primary TC and the upstream trough results in local jet-streak formation and the initial amplification of the downstream midlatitude waveguide (Figs. 7c, 8c). This initial flow reconfiguration is associated with midtropospheric descent implied by convergent upper-tropospheric wind equatorward and on the eastern flank of the immediate downstream ridge (Figs. 7c, 8c), which can inhibit the formation of deep, moist convection and promote the intrusion of dry air from aloft into any TCs in the vicinity (Gray 1968). In the context of the ventilation index, anomalously high ventilation index values are aligned along a meridional corridor following the poleward movement

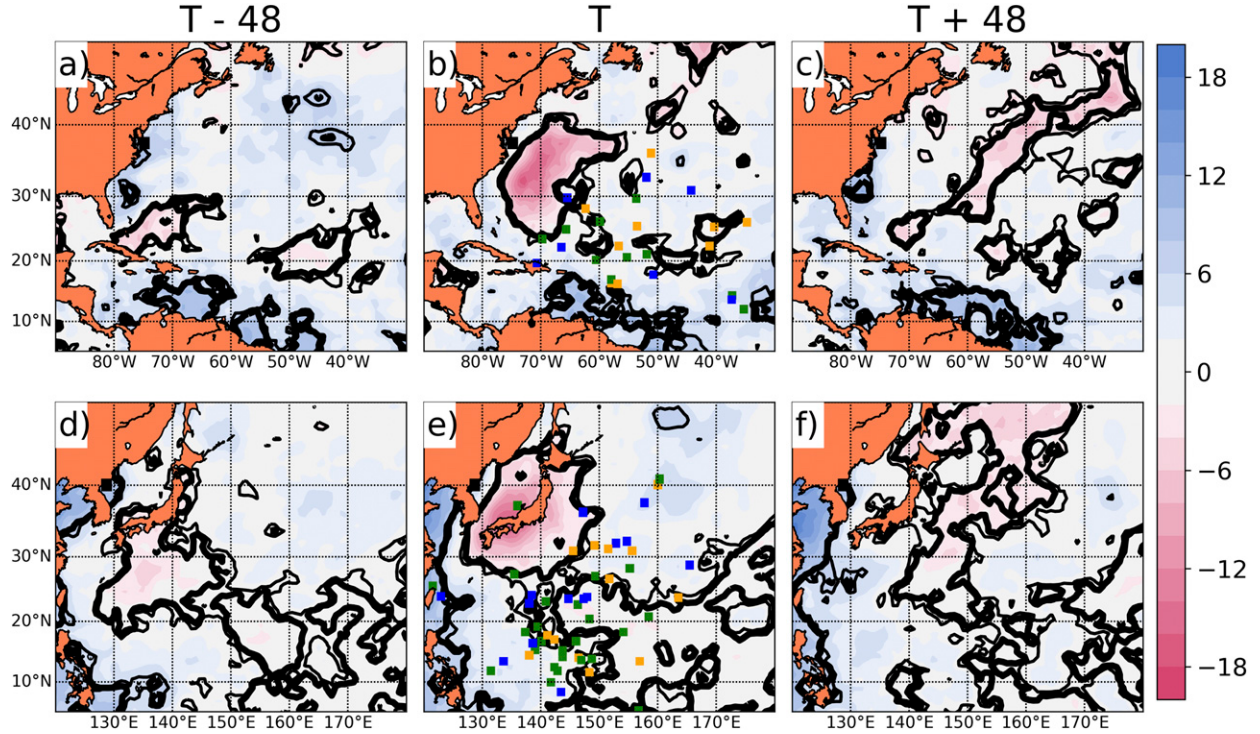


FIG. 10. As in Fig. 9, but for the MPI (units: m s^{-1} , shaded per the linear color bar at right) component of the ventilation index. Blue shading represents higher MPI and a more conducive environment to TC formation and maintenance and red shading represents lower MPI and a less conducive environment to TC formation and maintenance.

of the primary TCs (Figs. 9b,e). As at earlier times, the anomalously large ventilation index values result from anomalously weak composite-mean MPI (Figs. 10b,e) and anomalously high composite-mean entropy deficit (Figs. 11b,e), both of which are again a result of upwelling along the primary TCs' track, as well as anomalously high composite-mean 850–200 hPa vertical wind shear (Figs. 12b,e). Elsewhere, anomalously large 850–200 hPa vertical wind shear magnitude is found in both basins in association with the amplified midlatitude jet, primarily poleward of the amplified downstream ridge, and anomalously low 850–200 hPa vertical wind shear is found near the center of this ridge (Figs. 12b,e). In the western North Pacific, however, anomalously large vertical wind shear also extends equatorward of the downstream amplified ridge, encompassing the locations of many of the secondary TCs (Fig. 12e).

Within 24 h after the time of maximum interaction, anomalously large composite-mean 250–150 hPa layer averaged PV (to the 99% confidence level; not shown) extends to the southwest on the equatorward side of the downstream ridge in the North Atlantic (Fig. 7d), indicative of anticyclonic wave breaking (Thornicroft et al. 1993). This may suggest that the environment in which some secondary TCs are embedded becomes less conducive to TC development and maintenance, as anticyclonic

wave breaking and associated PV streamer formation can (depending on where a TC is located relative to these features) increase vertical wind shear and the associated intrusion of cool and dry midlatitude air into a TC's circulation (Galarneau et al. 2015; Zhang et al. 2017; Zhang and Wang 2018). Anticyclonic wave breaking is not evident in the western North Pacific composite (Fig. 8d), however, consistent with the longer, stronger midlatitude jet along the midlatitude waveguide being more resilient against Rossby wave breaking (Wirth et al. 2018).

By two days after the time of maximum interaction, there is a significant degradation in the signal in the North Atlantic, consistent with Pohorsky et al. (2019), associated with the termination of the initiated composite-mean Rossby wave packet due to wave breaking (Fig. 7e). Concurrently, many of the statistically significant impacts to the ventilation index and its components directly resulting from the interaction of the primary TCs with the midlatitude waveguide have moved well into the midlatitudes and/or become indistinct (Figs. 9c–c12c). In the western North Pacific, however, the downstream signal remains detectable through three days after the time of maximum interaction (Figs. 8e,f). Anomalously large ventilation indices remain present over the subtropical portion

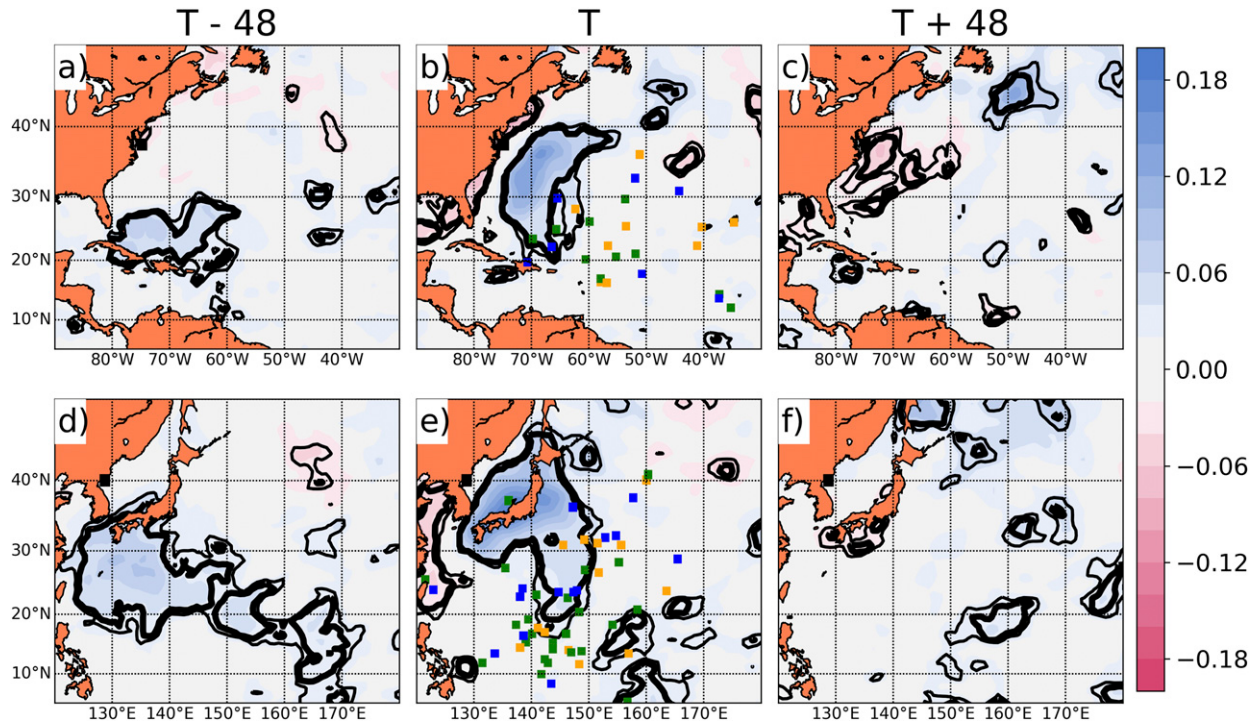


FIG. 11. As in Fig. 9, but for the entropy deficit (units: nondimensional; shaded per the linear color bar at right) component of the ventilation index. Blue shading represents larger entropy deficits representative of a less conducive environment to TC formation and maintenance and red shading represents smaller entropy deficit values representative of a more conducive environment to TC formation and maintenance.

of the western North Pacific (Fig. 9f), which at this time are almost exclusively the result of anomalously large vertical wind shear equatorward of the first downstream ridge (Fig. 12f).

b. Composite-mean secondary-TC-centered environments

Although the interaction of a primary TC with the midlatitude waveguide results in the amplification of the composite-mean downstream pattern, there is significant variability in secondary TC locations (colored squares in Figs. 9b and 9e) relative to the midlatitude pattern. This motivates a composite analysis centered on the secondary TCs. For this analysis, secondary TCs are stratified by whether they intensified or weakened (here defined by whether their minimum sea level pressure decreases or increases, respectively, by at least 5 hPa) over the 96-h period centered on the time of maximum interaction. As is shown below, this analysis demonstrates how the *position* of a secondary TC relative to the amplified midlatitude waveguide, more so than details of the waveguide's amplification (e.g., wave-breaking or lack thereof, amplitude, latitude of waveguide, etc.), exerts the largest control on the outcome of an indirect-interaction event on a secondary TC's intensity. However,

note that this analysis only establishes association and thus does not establish *causation*; i.e., the secondary TCs do not necessarily change intensity *as a result* of the indirect-interaction events.

In the North Atlantic, secondary TCs that intensify following an indirect-interaction event are equatorward of the downstream (relative to the primary TCs) ridge (Figs. 5b, 13a–c) in a low-to-moderate shear environment well-removed from the midlatitude waveguide (Table 3 and Figs. 13a–c). Conversely, secondary TCs that weaken following an indirect-interaction event are displaced southeast of the downstream ridge, closer to the midlatitude waveguide in a moderate-shear environment (Table 3 and Figs. 14a–c), through the time of maximum interaction (Figs. 5a, 14a,b). This impact is consistent with that for the case of North Atlantic TC Jose (2017), which is included within this composite subset, in Fig. 1, and for North Atlantic TCs Earl, Fiona, and Gaston (2010) described by Fowler and Galarneau (2017). Only by 48 h after the time of maximum interaction are these TCs situated equatorward of the downstream ridge (Fig. 14c). Additionally, the presence of a large negative PV anomaly north of the secondary TCs at 48 h before the time of maximum interaction for the strengthening storms may enhance

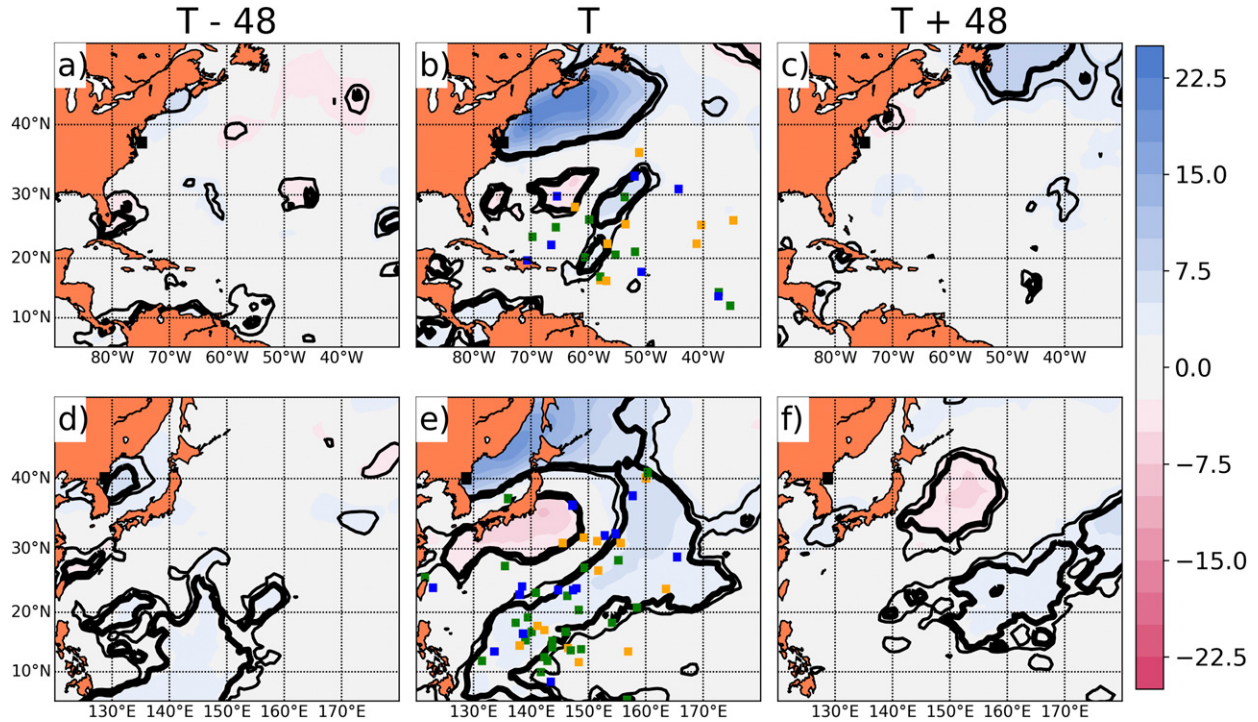


FIG. 12. As in Fig. 9, but for the 850–200 hPa vertical wind shear magnitude (units: m s^{-1} ; shaded per the linear color bar at right) component of the ventilation index. Blue shading represents larger 850–200 hPa vertical wind shear values representative of a less conducive environment to TC formation and maintenance and red shading represents smaller 850–200 hPa vertical wind shear values representative of a more conducive environment to TC formation and maintenance.

easterly flow on the north side of the TC thus advecting moisture to the up-shear (west) side of the TC (Figs. 13a,d). This may act to insulate the TC from dry air intrusion incurred by the indirect interaction (Galarneau et al. 2015).

In the western North Pacific, weakening versus strengthening secondary TCs primarily stratify by latitude, with strengthening secondary TCs being located significantly farther south, farther away from the midlatitude waveguide in a weaker-shear environment, as compared to their weakening counterparts (Table 4; Figs. 5c, 5d, 13d–f, and 14d–f). In these strengthening cases, the large-scale flow amplification is confined to latitudes poleward of the secondary TCs, such that these secondary TCs could be considered to *not* be indirect-interaction events given the apparent lack of impact of the primary TCs on these secondary TCs' environments. In contrast, the composite-mean signal for the weakening secondary TCs in the western North Pacific suggests that at least some of these TCs are interacting with the midlatitude waveguide themselves, as evidenced by the downstream ridge building from the composite-mean secondary TC position two days after the time of maximum interaction (Fig. 14f). Case-study analysis is necessary to

document the extent to which the flow reconfiguration downstream of the primary TCs contributes to these weakening secondary TCs, however.

5. Impacts to primary and secondary TC track and intensity predictability

The previous two sections have demonstrated the large-scale flow reconfiguration resulting from the interaction of a primary TC with the midlatitude waveguide and the conditions under which secondary TCs typically intensify or weaken during the indirect-interaction process. Given the basin-wide reduction in medium-range predictability for forecasts initialized one to two (or more) days prior to the interaction of a TC with the midlatitude waveguide (e.g., Harr and Archambault 2016); however, it is unclear as to the extent that these secondary TC outcomes are predictable. In this section, official track and intensity forecasts issued 24–48 h prior to time of maximum interaction are verified for both primary and secondary TCs to provide an answer (at least in part) to this question.

In terms of official track forecasts, forecasts of both primary and secondary TC tracks have slightly reduced

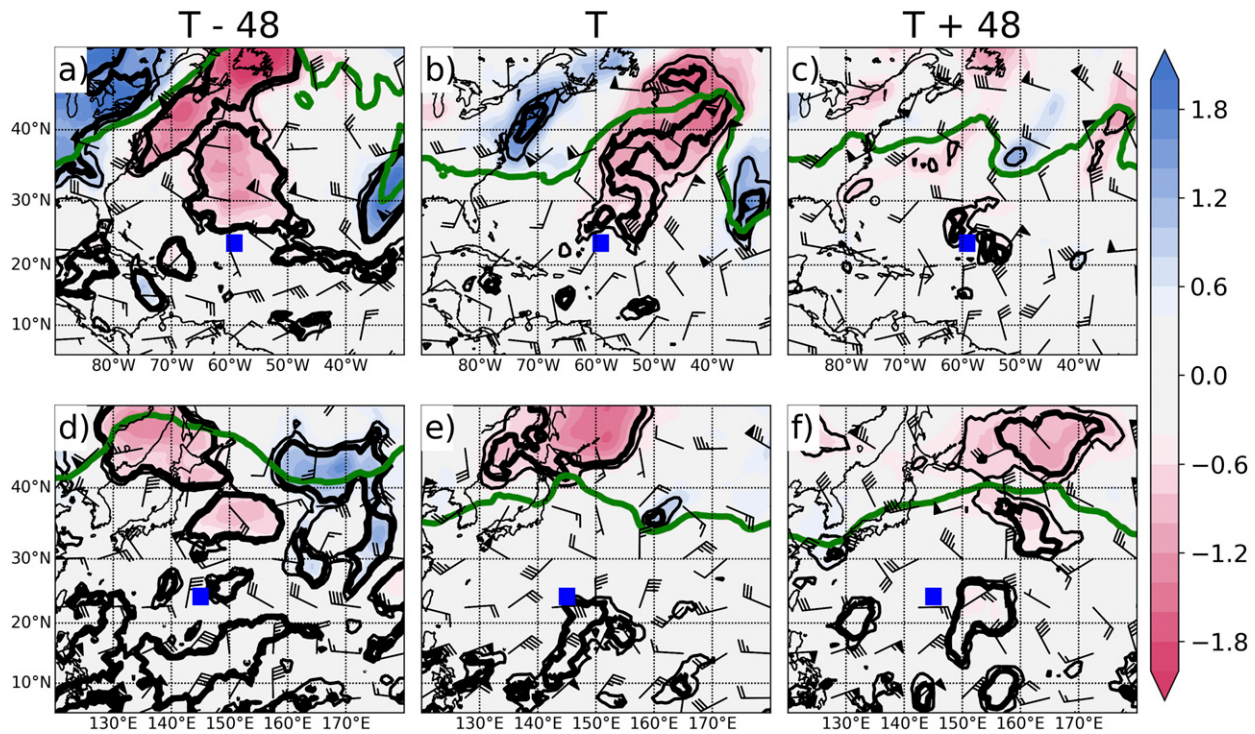


FIG. 13. Secondary-TC-centered composite-mean PV anomalies on the 340-K isentropic surface every 48 h from (a),(d) 48 h before the time of maximum interaction to (c),(f) 48 h after the time of maximum interaction for all strengthening secondary TCs (as given by the green squares in Figs. 9b and 9e). The wind bars represent the 850–200 hPa wind shear magnitude (bars; half-flag: 5 kt, flag: 10 kt, pennant: 50 kt). The thin black line denotes anomalies that are statistically significant to at least 95% confidence and the thick black line denotes anomalies that are statistically significant to at least 99% confidence. The thick green line represents the composite-mean 2-PVU isoline on the 340-K isentropic surface averaged over all strengthening cases in each respective basin at each time. (a)–(c) The North Atlantic composite and (d)–(f) the western North Pacific composite. The blue squares represent the average location of all secondary strengthening TCs at each time. The anomalies are computed by comparing raw values vs a climatology defined using a 15-day average centered on the date of each indirect-interaction event (the time of maximum interaction) over the period 1980–2010.

predictability compared to climatology through 48 h after forecast issuance, but not to the 95% confidence level (Figs. 15a,c). However, consistent with previous studies (McTaggart-Cowan et al. 2007; Fowler and Galarneau 2017), official forecast track errors for the primary and secondary TCs in the western North Pacific and the secondary TCs in the North Atlantic are associated with significantly reduced predictability between 72 and 96 h after forecast issuance (Figs. 15a,c). While the cause for these increased errors is not immediately clear, one possibility is inaccuracies in forecasting the interaction of the primary TC with the upstream trough, which is well-known to be a significant source of forecast error in forecasts initialized prior to the time of maximum interaction (e.g., Komaromi et al. 2011; Scheck et al. 2011; Riemer and Jones 2014; Harr and Archambault 2016; Keller et al. 2019). In these forecasts, small errors in numerical model forecasts originating near the interaction point between the primary TC and

midlatitude waveguide can propagate downstream and grow, ultimately impacting the skill of official track forecasts that are partially based off of numerical model forecasts.

Conversely, in terms of official intensity forecasts, only forecasts of North Atlantic primary TCs verifying at 12–48 h after forecast issuance are associated with reduced predictability compared to climatology (Fig. 15b). In fact, in the western North Pacific, both the primary and secondary TCs are associated with statistically significantly *increased* predictability at 72, 96, and 120 h (Fig. 15d). This is an unexpected result, particularly given the significantly reduced track predictability at these lead times (Fig. 15b). However, the sample sizes at these forecast times (particularly 96 and 120 h) are very small, such that only a few TCs (which may be outliers) contribute to the results shown (Fig. 15). While preliminary findings suggest very little correlation between increased wind shear and increased predictability of the downstream TCs,

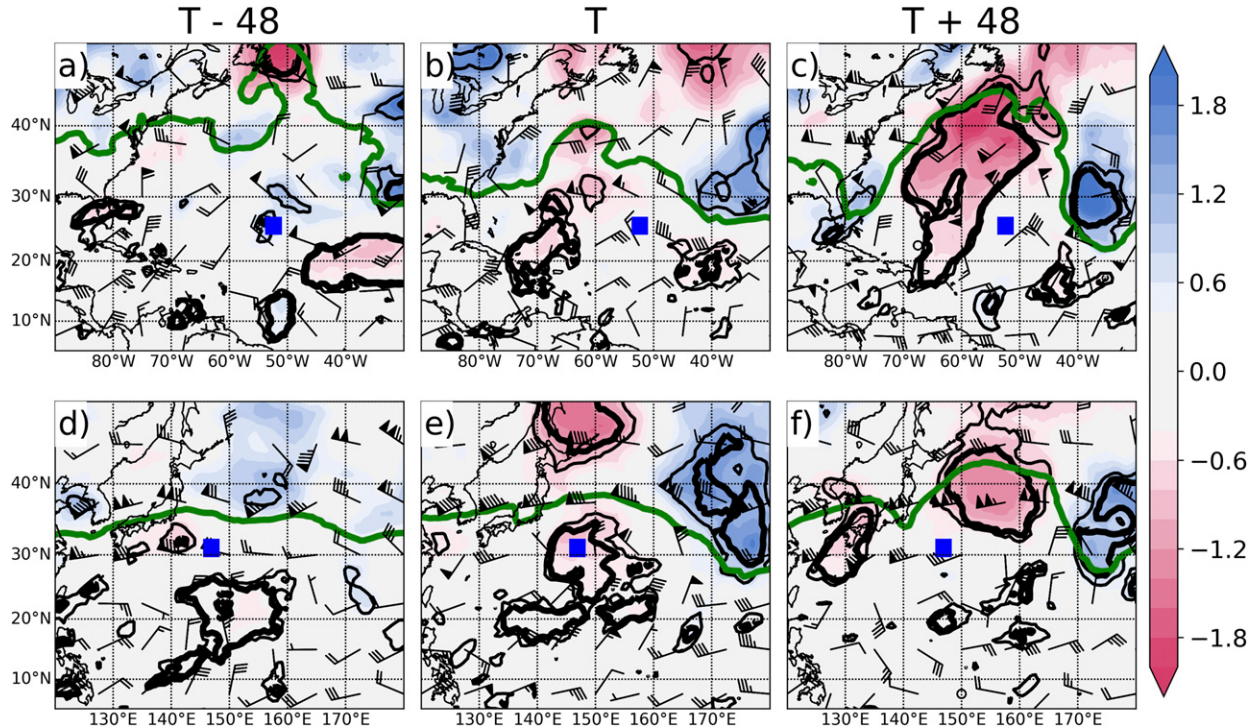


FIG. 14. As in Fig. 13, but for all weakening TCs (as given by the blue squares in Figs. 9b and 9e).

potential future research could determine whether TCs in regions of large tropospheric-deep wind shear are slightly more predictable due to the high likelihood that the TC will weaken given that other parameters important to intensification/maintenance are not met (e.g., warm SSTs and high midtropospheric water content; Rios-Berrios and Torn 2017) or not. Additionally, while a diagnosis of the secondary storms does not reveal a correlation between improved forecast skill with storms that systematically weakened postinteraction, there is an average improvement in skill [with respect to baseline forecasts from the Operational Intensity blend of the climatology and persistence and decay (OCD5) statistical hurricane intensity forecast (SHIFOR) models for the North Atlantic and from the 5 day statistical typhoon intensity forecast (STIFOR) ST5D model in the western North Pacific] of approximately 40% at later forecast times (particularly 72 and 96 h).

6. Conclusions and future work

Substantial research has been published on the interaction of TCs with the midlatitude flow as they recurve into the midlatitudes and undergo ET, including the associated reduction in downstream midlatitude predictability. Separately, others have published on the

concurrence of multiple TCs within a given basin. However, only a limited number of case studies have been conducted to examine the influence, direct or indirect, that a recurring TC can have on the downstream subtropical to tropical environment, including secondary TCs located within such environments. This study represents an attempt to bridge this divide by creating a climatology of indirect TC interaction events facilitated by TC–waveguide interaction and using this climatology to document the associated flow reconfiguration in proximity to the secondary TCs.

Over the 30-yr period between 1989 and 2018, 26 and 56 indirect interactions are identified in the North Atlantic (Table 1) and western North Pacific (Table 2) basins, respectively. Consistent with previous studies (as synthesized in Keller et al. 2019) of TC–waveguide interactions, the interaction of a primary TC with the midlatitude waveguide results in significant downstream *midlatitude* flow reconfiguration, most notably in the amplification of the immediate downstream ridge, with impacts lasting up to two to three days after the time of maximum interaction (Fig. 16). However, with the exception of increased vertical wind shear equatorward of the amplified downstream ridge in the western North Pacific (Figs. 12d–f), most of the associated environmental impacts are confined to the midlatitudes. Additionally, it was found that while upwelling from

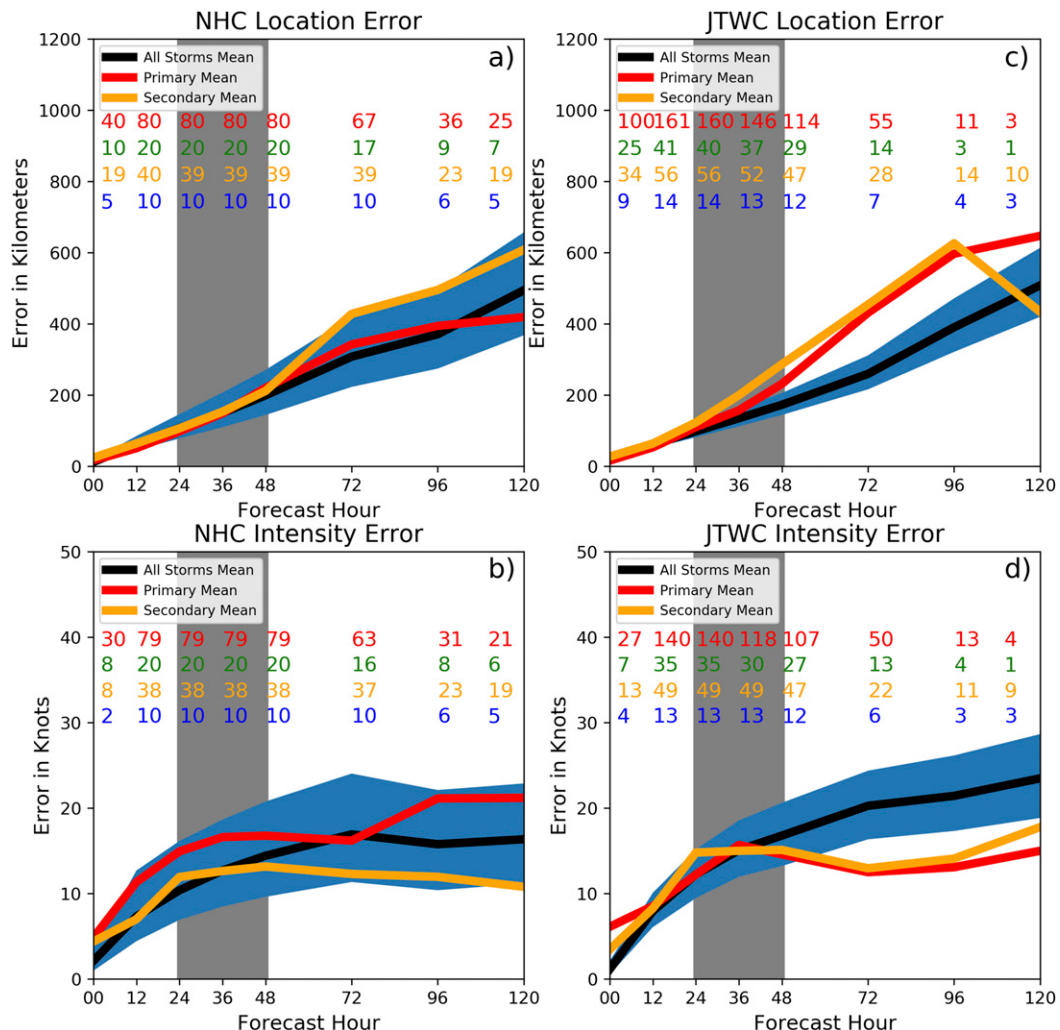


FIG. 15. NHC-forecast (a) track (great-circle distance in km) and (c) intensity (kt) error for all cases of all forecasts of primary (red) and secondary (orange) TCs initialized between 48 to 24 h before the time of maximum interaction. The red and orange numbers represent the number of valid forecasts at that forecast lead time for the primary and secondary TCs, respectively. The green and blue numbers represent the number of TCs used in the averaging at that forecast lead time for the primary and secondary TCs, respectively. The black lines represent the mean error and the blue shading represents the 2.5th–97.5th percentiles of errors for all 1989–2018 TCs excluding the primary and secondary TCs (following the procedure described in section 2f). (b),(d) As in (a),(c), but for JTWC official forecasts. The 0-h forecast counts in this figure are lower due to the limited availability of these data.

the primary TCs can impact the environment immediately surrounding them, there are no impacts to the secondary TCs (not shown). This negligible impact is likely due to the fact that the secondary TCs do not usually follow a similar track to their corresponding initial TCs.

This study identifies two pathways by which a secondary TC can weaken following an indirect-interaction event. In the Atlantic, weakening secondary TCs are closer to the midlatitude waveguide on the southeastern edge of the amplified midlatitude ridge (consistent with

Fowler and Galarneau 2017), whereas strengthening secondary TCs are further from the waveguide and equatorward of the amplified midlatitude ridge (Table 3; Fig. 16, bottom left). Conversely, western North Pacific strengthening and weakening secondary TCs are primarily stratified by latitude, with weakening secondary TCs located nearly 6° latitude poleward of their strengthening secondary TC counterparts at the time of maximum interaction, as opposed to their positions relative to the midlatitude pattern (Fig. 16, bottom right). Strengthening secondary TCs remain

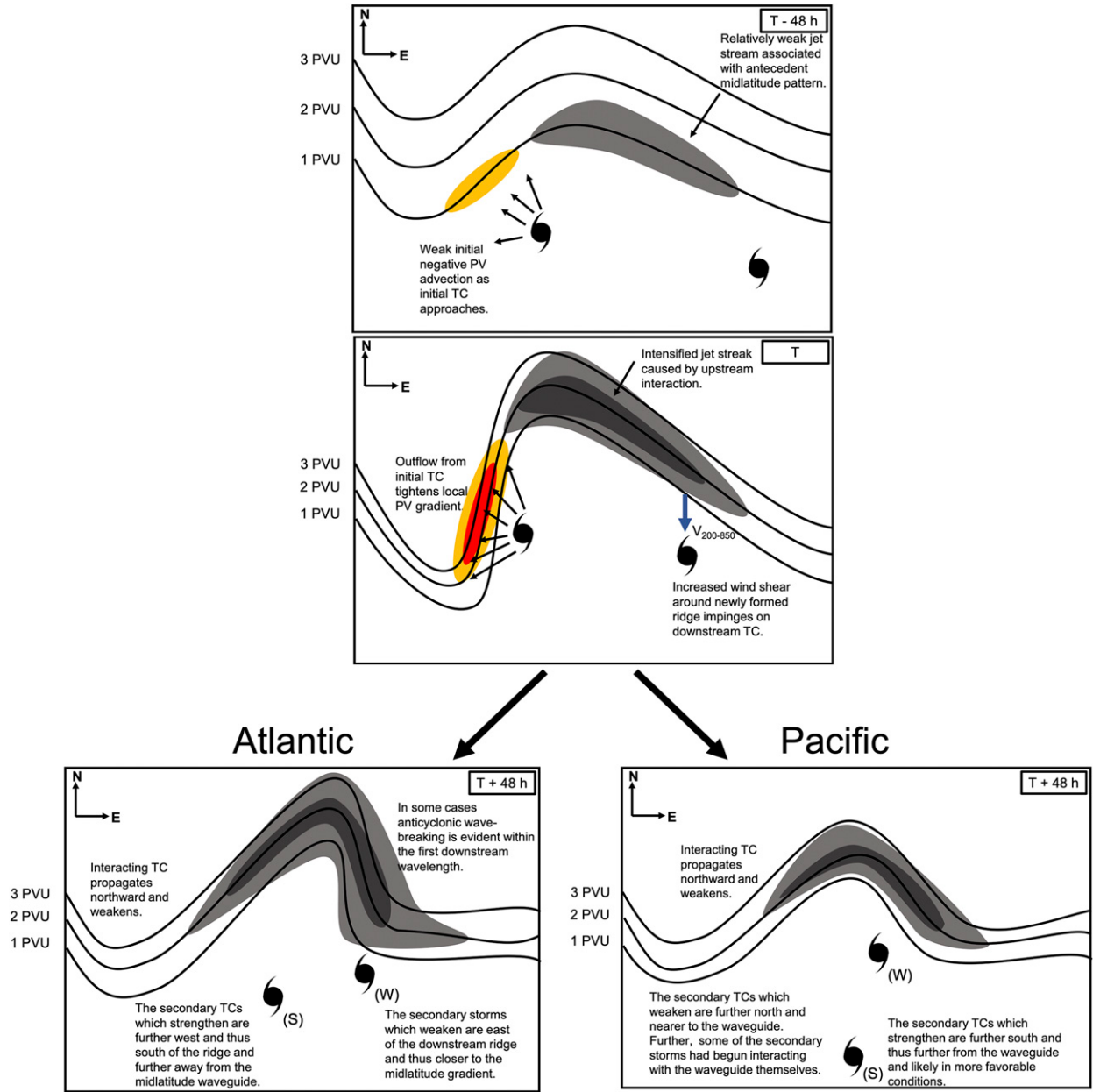


FIG. 16. Conceptual schematic of the downstream flow reconfiguration and associated environmental changes associated with a primary TC's interaction with the midlatitude waveguide every 48 h between (top) 48 h before the time of maximum interaction and (bottom) 48 h after the time of maximum interaction. Black vectors denote the upper-tropospheric irrotational wind, orange and red shading denotes increasing levels of negative PV advection by the upper-tropospheric irrotational wind, and gray shading denotes increasing upper-tropospheric wind speed. The bottom row is split between the North Atlantic and western North Pacific basins to highlight key differences between the two basins.

well-equatorward of the midlatitude waveguide and are largely unaffected by changes in the midlatitude flow, whereas weakening secondary TCs rapidly approach the midlatitude waveguide following the time of maximum interaction (Table 4; Fig. 16, bottom right). This insight can foster increased forecaster situational awareness during future indirect-interaction events

that may allow them to make more-skillful secondary-TC intensity forecasts during and after the time of maximum interaction. That said, it is arguable as to the extent that the primary TCs' interaction with the midlatitude waveguide influences these outcomes in either basin; the outcomes depicted herein are merely associative rather than causative in the absence of

case-study analyses utilizing numerical-model simulations with piecewise PV inversion techniques.

By definition, indirect-interaction events require there to be multiple concurrent TCs within a given basin, the likelihood of which is strongly governed by the seasonal cycle and modulated by subseasonal modes of variability such as the Madden–Julian oscillation (MJO) and convectively coupled equatorial waves (Schenkel 2016 and references therein). The extent to which these modes of variability project on the synoptic-scale midlatitude pattern before, during, and after an indirect-interaction event is unclear, however. That said, using archived MJO index data from the Australian Bureau of Meteorology, a significant portion of the western North Pacific interactions occur when the MJO is in phases 6 or 7 (not shown), consistent with previous research connecting increased TC activity in this basin to these MJO phases (Li and Zhou 2013; Klotzbach 2014). Likewise, most North Atlantic indirect-interaction events occur when the MJO is in phases 1 or 2 (not shown), which is also consistent with previous works connecting increased TC activity in the North Atlantic to these MJO phases (Klotzbach 2010, 2014). Thus, in both basins, indirect-interaction events are more frequent when multiple TCs themselves are more frequent. Further research is necessary to quantify the MJO’s impact, if any, on the flow reconfigurations associated with these indirect-interaction events, however.

The analyses presented in this research motivate further research to better document indirect-interaction events and their impacts on secondary TCs’ track and intensity. For instance, case studies are necessary to quantify the extent to which the primary TC in each case contributes to the subsequent downstream flow evolution and secondary TC track and intensity. Techniques such as piecewise PV inversion (e.g., Grams et al. 2013a,b), analog compositing (Pohorsky et al. 2019), and ensemble-based sensitivity analysis (e.g., Torn and Hakim 2015; Torn 2016), each as applied to the primary TC and/or antecedent midlatitude pattern, can be used to diagnose such sensitivities. Research is under way to do so for the indirect interaction between North Atlantic TCs Irma and Jose in 2017 described in section 1. Further, the use of the negative PV advection by the irrotational wind metric to identify indirect-interaction events leaves out other potential indirect-interaction pathways, including through Rossby wave radiation (Schenkel 2016, 2017; Krouse et al. 2008) and primary-TC outflow into an upper-tropospheric low that is located in close proximity to

another TC (e.g., TCs Rita and Philippe in 2005; Franklin 2006). This could motivate further research to diagnose the relative occurrence and importance of each pathway not only in the indirect interactions identified here but in a larger set of cases. Further, the forecast-error analysis presented herein focuses only on forecasts issued by official warning centers, which represent expert syntheses of a wide range of available model guidance and observational data. However, numerical modeling systems likely have varying skill for these events (e.g., Keller et al. 2011), and future research to quantify such skill variations may provide insight into the synoptic-scale conditions and/or model configuration parameters that lead to particularly enhanced or degraded forecast skill. Finally, the sample sizes of indirect-interaction events in both basins are small, and the subsets of events by the secondary TCs’ intensity evolution are even smaller. Future research using a longer climatology (albeit subject to increasingly large uncertainty at earlier times) and/or global coupled ocean-atmosphere model output is warranted to constrain the analysis uncertainty resulting from these small sample sizes.

Acknowledgments. This research greatly benefited from conversations with and input from Heather Archambault (Citadel), Lance Bosart (University at Albany), Tom Galarneau (University of Oklahoma/CIMMS), Sergey Kravtsov (UWM), Peter Finocchio (NRC), Michael Riemer (Johannes Gutenberg University at Mainz), Paul Roebber (UWM), Benjamin Schenkel (University of Oklahoma/CIMMS), and Brian Tang (University at Albany). The authors thank Will Komaromi, Editor Kristen Corbosiero, and two anonymous reviewers for their thoughtful and detailed suggestions that substantially improved the quality of the work.

Data availability statement. The ERA-Interim data used in this study are available from the ECMWF’s Meteorological Archival and Retrieval System at <https://apps.ecmwf.int/datasets/data/interim-full-daily/levtype=sfc/>. The NOAA 0.25° optimum interpolation SST data used in this study are available from <https://psl.noaa.gov/data/gridded/data.noaa.oisst.v2.html>. The NHC best track and archived forecast data used in this study are available from <https://www.nhc.noaa.gov/data/>. The JTWC best track and archived forecast data used in this study are available from <https://www.metoc.navy.mil/jtvc/jtvc.html>. Finally, the MJO index data used in this study are available from <http://www.bom.gov.au/climate/mjo/graphics/rmm.74toRealtime.txt>.

REFERENCES

- Agustí-Panareda, A., C. D. Thorncroft, G. C. Craig, and S. L. Gray, 2004: The extratropical transition of Hurricane Irene (1999): A potential-vorticity perspective. *Quart. J. Roy. Meteor. Soc.*, **130**, 1047–1074, <https://doi.org/10.1256/qj.02.140>.
- , S. L. Gray, G. C. Craig, and C. Thorncroft, 2005: The extratropical transition of Tropical Cyclone Lili (1996) and its crucial contribution to a moderate extratropical development. *Mon. Wea. Rev.*, **133**, 1562–1573, <https://doi.org/10.1175/MWR2935.1>.
- Aiyer, A., 2015: Recurring western North Pacific tropical cyclones and midlatitude predictability. *Geophys. Res. Lett.*, **42**, 7799–7807, <https://doi.org/10.1002/2015GL065082>.
- Anwender, D., P. A. Harr, and S. C. Jones, 2008: Predictability associated with the downstream impacts of the extratropical transition of tropical cyclones: Case studies. *Mon. Wea. Rev.*, **136**, 3226–3247, <https://doi.org/10.1175/2008MWR2249.1>.
- , S. C. Jones, M. Leutbecher, and P. A. Harr, 2010: Sensitivity experiments for ensemble forecasts of the extratropical transition of Typhoon Tokage (2004). *Quart. J. Roy. Meteor. Soc.*, **136**, 183–200, <https://doi.org/10.1002/qj.527>.
- Archambault, H. M., L. F. Bosart, D. Keyser, and J. M. Cordeira, 2013: A climatological analysis of the extratropical flow response to recurring western North Pacific tropical cyclones. *Mon. Wea. Rev.*, **141**, 2325–2346, <https://doi.org/10.1175/MWR-D-12-00257.1>.
- , D. Keyser, L. F. Bosart, C. A. Davis, and J. M. Cordeira, 2015: A composite perspective of the extratropical flow response recurring western North Pacific tropical cyclones. *Mon. Wea. Rev.*, **143**, 1122–1141, <https://doi.org/10.1175/MWR-D-14-00270.1>.
- Banzon, V., T. M. Smith, T. M. Chin, C. Liu, and W. Hankins, 2016: A long-term record of blended satellite and in situ sea-surface temperature for climate monitoring, modeling and environmental studies. *Earth Syst. Sci. Data*, **8**, 165–176, <https://doi.org/10.5194/essd-8-165-2016>.
- Berg, R., 2018: National Hurricane Center Tropical Cyclone Report: Hurricane Jose (5–22 September 2017). Tech. Rep. AL122017, National Hurricane Center, 36 pp., https://www.nhc.noaa.gov/data/tcr/AL122017_Jose.pdf.
- Bosart, L. F., 2003: Tropopause folding: Upper-level frontogenesis, and beyond. *A Half Century of Progress in Meteorology: A Tribute to Richard Reed*, Meteor. Monogr., No. 31, Amer. Meteor. Soc., 13–47.
- Colbert, A. J., and B. J. Soden, 2012: Climatological variations in North Atlantic tropical cyclone tracks. *J. Climate*, **25**, 657–673, <https://doi.org/10.1175/JCLI-D-11-00034.1>.
- Cunningham, P., and D. Keyser, 2000: Analytical and numerical modelling of jet streaks: Barotropic dynamics. *Quart. J. Roy. Meteor. Soc.*, **126**, 3187–3217, <https://doi.org/10.1002/qj.49712657010>.
- Dee, D. P., and Coauthors, 2011: The ERA-Interim reanalysis: Configuration and performance of the data assimilation system. *Quart. J. Roy. Meteor. Soc.*, **137**, 553–597, <https://doi.org/10.1002/qj.828>.
- Efron, B., and R. Tibshirani, 1994: *An Introduction to the Bootstrap*. Chapman & Hall, 456 pp.
- Evans, C., and Coauthors, 2017: The extratropical transition of tropical cyclones. Part I: Cyclone evolution and direct impacts. *Mon. Wea. Rev.*, **145**, 4317–4344, <https://doi.org/10.1175/MWR-D-17-0027.1>.
- Finocchio, P. M., and J. D. Doyle, 2019: How the speed and latitude of the jet stream affect the downstream response to recurring tropical cyclones. *Mon. Wea. Rev.*, **147**, 3261–3281, <https://doi.org/10.1175/MWR-D-19-0049.1>.
- Fischer, M. S., B. H. Tang, and K. L. Corbosiero, 2017: Assessing the influence of upper-tropospheric troughs on tropical cyclone intensification rates after genesis. *Mon. Wea. Rev.*, **145**, 1295–1313, <https://doi.org/10.1175/MWR-D-16-0275.1>.
- Fowler, J. P., and T. J. Galarneau, 2017: Influence of storm–storm and storm–environment interactions on tropical cyclone formation and evolution. *Mon. Wea. Rev.*, **145**, 4855–4875, <https://doi.org/10.1175/MWR-D-17-0131.1>.
- Franklin, J. L., 2006: Tropical cyclone report: Hurricane Philippe (2005). Tech. Rep. AL172005, National Hurricane Center, 10 pp., https://www.nhc.noaa.gov/data/tcr/AL172005_Philippe.pdf.
- Fujiwhara, S., 1921: The natural tendency towards symmetry of motion and its application as a principle in meteorology. *Quart. J. Roy. Meteor. Soc.*, **47**, 287–292, <https://doi.org/10.1002/qj.4970472010>.
- Galarneau, T. J., Jr., and C. A. Davis, 2013: Diagnosing forecast errors in tropical cyclone motion. *Mon. Wea. Rev.*, **141**, 405–430, <https://doi.org/10.1175/MWR-D-12-00071.1>.
- , R. McTaggart-Cowan, L. F. Bosart, and C. A. Davis, 2015: Development of North Atlantic tropical disturbances near upper-level potential vorticity streamers. *J. Atmos. Sci.*, **72**, 572–597, <https://doi.org/10.1175/JAS-D-14-0106.1>.
- Grams, C. M., and H. M. Archambault, 2016: The key role of diabatic outflow in amplifying the midlatitude flow: A representative case study of weather systems surrounding western North Pacific extratropical transition. *Mon. Wea. Rev.*, **144**, 3847–3869, <https://doi.org/10.1175/MWR-D-15-0419.1>.
- , and Coauthors, 2011: The key role of diabatic processes in modifying the upper-tropospheric wave guide: A North Atlantic case-study. *Quart. J. Roy. Meteor. Soc.*, **137**, 2174–2193, <https://doi.org/10.1002/qj.891>.
- , S. C. Jones, C. A. Davis, P. A. Harr, and M. Weissmann, 2013a: The impact of Typhoon Jangmi (2008) on the midlatitude flow. Part I: Upper-level ridgebuilding and modification of the jet. *Quart. J. Roy. Meteor. Soc.*, **139**, 2148–2164, <https://doi.org/10.1002/qj.2091>.
- , —, and —, 2013b: The impact of Typhoon Jangmi (2008) on the midlatitude flow. Part II: Downstream evolution. *Quart. J. Roy. Meteor. Soc.*, **139**, 2165–2180, <https://doi.org/10.1002/qj.2119>.
- , S. T. K. Lang, and J. H. Keller, 2015: A quantitative assessment of the sensitivity of the downstream midlatitude flow response to extratropical transition of tropical cyclones. *Geophys. Res. Lett.*, **42**, 9521–9529, <https://doi.org/10.1002/2015GL065764>.
- Gray, W. M., 1968: Global view of the origin of tropical disturbances and storms. *Mon. Wea. Rev.*, **96**, 669–700, [https://doi.org/10.1175/1520-0493\(1968\)096<0669:GVOTOO>2.0.CO;2](https://doi.org/10.1175/1520-0493(1968)096<0669:GVOTOO>2.0.CO;2).
- Harr, P. A., and J. M. Dea, 2009: Downstream development associated with the extratropical transition of tropical cyclones over the western North Pacific. *Mon. Wea. Rev.*, **137**, 1295–1319, <https://doi.org/10.1175/2008MWR2558.1>.
- , and H. M. Archambault, 2016: Dynamics, predictability, and high-impact weather associated with the extratropical transition of tropical cyclones. *Dynamics and Predictability of Large-Scale, High-Impact Weather and Climate Events*, J. Li et al., Eds., Cambridge University Press, 153–167, <https://doi.org/10.1017/CBO9781107775541.013>.

- Hart, R. E., R. N. Maue, and M. C. Watson, 2007: Estimating local memory of tropical cyclones through MPI anomaly evolution. *Mon. Wea. Rev.*, **135**, 3990–4005, <https://doi.org/10.1175/2007MWR2038.1>.
- Hodges, K., D. Anwender, and S. C. Jones, 2008: Predictability associated with the downstream impacts of the extratropical transition of tropical cyclones: Methodology and a case study of Typhoon Nabi (2005). *Mon. Wea. Rev.*, **136**, 3205–3225, <https://doi.org/10.1175/2008MWR2248.1>.
- Hoskins, B. J., M. E. McIntyre, and A. W. Robertson, 1985: On the use and significance of isentropic potential vorticity maps. *Quart. J. Roy. Meteor. Soc.*, **111**, 877–946, <https://doi.org/10.1002/qj.49711147002>.
- Jones, S. C., and Coauthors, 2003: The extratropical transition of tropical cyclones: Forecast challenges, current understanding, and future directions. *Wea. Forecasting*, **18**, 1052–1092, [https://doi.org/10.1175/1520-0434\(2003\)018<1052:TETOTC>2.0.CO;2](https://doi.org/10.1175/1520-0434(2003)018<1052:TETOTC>2.0.CO;2).
- JTWC, 2019: Best track data. Joint Typhoon Warning Center, accessed December 2018, [https://www.metoc.navy.mil/jtvc.html?western-pacific](https://www.metoc.navy.mil/jtwc/jtvc.html?western-pacific).
- Keller, J. H., 2017: Amplification of the downstream wave train during extratropical transition: Sensitivity studies. *Mon. Wea. Rev.*, **145**, 1529–1548, <https://doi.org/10.1175/MWR-D-16-0193.1>.
- , S. C. Jones, J. L. Evans, and P. A. Harr, 2011: Characteristics of the TIGGE multimodel ensemble prediction system in representing forecast variability associated with extratropical transition. *Geophys. Res. Lett.*, **38**, L12802, <https://doi.org/10.1029/2011GL047275>.
- , and Coauthors, 2019: The extratropical transition of tropical cyclones. Part II: Interaction with the midlatitude flow, downstream impacts, and implications for predictability. *Mon. Wea. Rev.*, **147**, 1077–1106, <https://doi.org/10.1175/MWR-D-17-0329.1>.
- Klotzbach, P. J., 2010: On the Madden–Julian oscillation–Atlantic hurricane relationship. *J. Climate*, **23**, 282–293, <https://doi.org/10.1175/2009JCLI2978.1>.
- , 2014: The Madden–Julian oscillation’s impacts on worldwide tropical cyclone activity. *J. Climate*, **27**, 2317–2330, <https://doi.org/10.1175/JCLI-D-13-00483.1>.
- Komaromi, W. A., and J. D. Doyle, 2018: On the dynamics of tropical cyclone and trough interactions. *J. Atmos. Sci.*, **75**, 2687–2709, <https://doi.org/10.1175/JAS-D-17-0272.1>.
- , S. J. Majumdar, and E. D. Rappin, 2011: Diagnosing initial condition sensitivity of Typhoon Sinlaku (2008) and Hurricane Ike (2008). *Mon. Wea. Rev.*, **139**, 3224–3242, <https://doi.org/10.1175/MWR-D-10-05018.1>.
- Krouse, K. D., A. H. Sobel, and L. M. Polvani, 2008: On the wavelength of the Rossby waves radiated by tropical cyclones. *J. Atmos. Sci.*, **65**, 644–654, <https://doi.org/10.1175/2007JAS2402.1>.
- Landsea, C. W., 2007: Counting Atlantic tropical cyclones back to 1900. *Eos, Trans. Amer. Geophys. Union*, **88**, 197–202, <https://doi.org/10.1029/2007EO180001>.
- , and J. L. Franklin, 2013: Atlantic hurricane database uncertainty and presentation of a new database format. *Mon. Wea. Rev.*, **141**, 3576–3592, <https://doi.org/10.1175/MWR-D-12-00254.1>.
- Li, R. C., and W. Zhou, 2013: Modulation of western North Pacific tropical cyclone activity by the ISO. Part II: Tracks and landfalls. *J. Climate*, **26**, 2919–2930, <https://doi.org/10.1175/JCLI-D-12-00211.1>.
- McTaggart-Cowan, R., L. F. Bosart, J. R. Gyakum, and E. H. Atallah, 2007: Hurricane Katrina (2005). Part II: Evolution and hemispheric impacts of a diabatically generated warm pool. *Mon. Wea. Rev.*, **135**, 3927–3949, <https://doi.org/10.1175/2007MWR2096.1>.
- Pantillon, F., J.-P. Chaboureau, C. Lac, and P. Mascart, 2013: On the role of a Rossby wave train during the extratropical transition of Hurricane Helene (2006). *Quart. J. Roy. Meteor. Soc.*, **139**, 370–386, <https://doi.org/10.1002/qj.1974>.
- Papin, P., 2017: Variations in potential vorticity streamer activity: Development pathways, environmental impacts, and links to tropical cyclone activity in the North Atlantic basin. Ph.D. dissertation, University at Albany, 225 pp. <https://search.proquest.com/docview/1978476273>.
- Peirano, C. M., K. L. Corbosiero, and B. H. Tang, 2016: Revisiting trough interactions and tropical cyclone intensity change. *Geophys. Res. Lett.*, **43**, 5509–5515, <https://doi.org/10.1002/2016GL069040>.
- Petterssen, S., and S. J. Smebye, 1971: On the development of extratropical cyclones. *Quart. J. Roy. Meteor. Soc.*, **97**, 457–482, <https://doi.org/10.1002/qj.49709741407>.
- Pohorsky, R., M. Röhlisberger, C. M. Grams, J. Riboldi, and O. Martius, 2019: The climatological impact of recurving North Atlantic tropical cyclones on downstream extreme precipitation events. *Mon. Wea. Rev.*, **147**, 1513–1532, <https://doi.org/10.1175/MWR-D-18-0195.1>.
- Quinting, J. F., and S. C. Jones, 2016: On the impact of tropical cyclones on Rossby wave packets: A climatological perspective. *Mon. Wea. Rev.*, **144**, 2021–2048, <https://doi.org/10.1175/MWR-D-14-0029.1>.
- Reynolds, R. W., T. M. Smith, C. Liu, D. B. Chelton, K. S. Casey, and M. G. Schlax, 2007: Daily high-resolution-blended analyses for sea surface temperature. *J. Climate*, **20**, 5473–5496, <https://doi.org/10.1175/2007JCLI1824.1>.
- Riboldi, J., C. M. Grams, M. Riener, and H. M. Archambault, 2019: A phase locking perspective on Rossby wave amplification and atmospheric blocking downstream of recurving western North Pacific tropical cyclones. *Mon. Wea. Rev.*, **147**, 567–589, <https://doi.org/10.1175/MWR-D-18-0271.1>.
- Riemer, M., and S. C. Jones, 2010: The downstream impact of tropical cyclones on a developing baroclinic wave in idealized scenarios of extratropical transition. *Quart. J. Roy. Meteor. Soc.*, **136**, 617–637, <https://doi.org/10.1002/qj.605>.
- , and —, 2014: Interaction of a tropical cyclone with a high-amplitude, midlatitude wave pattern: Waviness analysis, trough deformation, and track bifurcation. *Quart. J. Roy. Meteor. Soc.*, **140**, 1362–1376, <https://doi.org/10.1002/qj.2221>.
- Rios-Berrios, R., and R. D. Torn, 2017: Climatological analysis of tropical cyclone intensity changes under moderate vertical wind shear. *Mon. Wea. Rev.*, **145**, 1717–1738, <https://doi.org/10.1175/MWR-D-16-0350.1>.
- Ritchie, E. A., and R. L. Elsberry, 2003: Simulations of the extratropical transition of tropical cyclones: Contributions by the midlatitude upper-level trough to re intensification. *Mon. Wea. Rev.*, **131**, 2112–2128, [https://doi.org/10.1175/1520-0493\(2003\)131<2112:SOTETO>2.0.CO;2](https://doi.org/10.1175/1520-0493(2003)131<2112:SOTETO>2.0.CO;2).
- , and —, 2007: Simulations of the extratropical transition of tropical cyclones: Phasing between the upper-level trough and tropical cyclones. *Mon. Wea. Rev.*, **135**, 862–876, <https://doi.org/10.1175/MWR3303.1>.
- Scheck, L., S. C. Jones, and M. Juckes, 2011: The resonant interaction of a tropical cyclone and a tropopause front in a barotropic model. Part II: Frontal waves. *J. Atmos. Sci.*, **68**, 420–429, <https://doi.org/10.1175/2010JAS3483.1>.

- Schenkel, B. A., 2016: A climatology of multiple tropical cyclone events. *J. Climate*, **29**, 4861–4883, <https://doi.org/10.1175/JCLI-D-15-0048.1>.
- , 2017: Are multiple tropical cyclone events similar among basins? *J. Climate*, **30**, 5805–5813, <https://doi.org/10.1175/JCLI-D-17-0088.1>.
- , and R. E. Hart, 2015: An examination of the thermodynamic impacts of western North Pacific tropical cyclones on their tropical tropospheric environment. *J. Climate*, **28**, 7529–7560, <https://doi.org/10.1175/JCLI-D-14-00780.1>.
- Tang, B., and K. Emanuel, 2012: A ventilation index for tropical cyclones. *Bull. Amer. Meteor. Soc.*, **93**, 1901–1912, <https://doi.org/10.1175/BAMS-D-11-00165.1>.
- Thorncroft, C. D., B. J. Hoskins, and M. E. McIntyre, 1993: Two paradigms of baroclinic-wave life-cycle behaviour. *Quart. J. Roy. Meteor. Soc.*, **119**, 17–55, <https://doi.org/10.1002/qj.49711950903>.
- Torn, R. D., 2016: Evaluation of atmosphere and ocean initial condition uncertainty and stochastic exchange coefficients on ensemble tropical cyclone intensity forecasts. *Mon. Wea. Rev.*, **144**, 3487–3506, <https://doi.org/10.1175/MWR-D-16-0108.1>.
- , and G. J. Hakim, 2015: Comparison of wave packets associated with extratropical transition and winter cyclones. *Mon. Wea. Rev.*, **143**, 1782–1803, <https://doi.org/10.1175/MWR-D-14-0006.1>.
- Wirth, V., M. Riemer, E. K. Chang, and O. Martius, 2018: Rossby wave packets on the midlatitude waveguide—A review. *Mon. Wea. Rev.*, **146**, 1965–2001, <https://doi.org/10.1175/MWR-D-16-0483.1>.
- Zhang, G., and Z. Wang, 2018: North Atlantic extratropical Rossby wave breaking during the warm season: Wave life cycle and role of diabatic heating. *Mon. Wea. Rev.*, **146**, 695–712, <https://doi.org/10.1175/MWR-D-17-0204.1>.
- , —, T. J. Dunkerton, M. S. Peng, and G. Magnusdottir, 2016: Extratropical impacts on Atlantic tropical cyclone activity. *J. Atmos. Sci.*, **73**, 1401–1418, <https://doi.org/10.1175/JAS-D-15-0154.1>.
- , —, M. Peng, and G. Magnusdottir, 2017: Characteristics and impacts of extratropical Rossby wave breaking during the Atlantic hurricane season. *J. Climate*, **30**, 2363–2379, <https://doi.org/10.1175/JCLI-D-16-0425.1>.